

Submitted to: *Special Issue of IEEE Transactions of Geoscience and Remote Sensing*
on "*Emerging Scatterometer Applications*"

SEASONAL TO INTERANNUAL VARIABILITY IN ANTARCTIC SEA-ICE SURFACE MELT

Mark R. Drinkwater and Xiang Liu
Jet Propulsion Laboratory
California Institute of Technology
Mail Stop 300-323
4800 Oak Grove Drive
Pasadena, CA 91109, USA

Corresponding Author: Mark R. Drinkwater
Tel: +001 818-354 8189
Fax: +001 818-393 6720

Email: M.Drinkwater@jpl.nasa.gov

April 8, 1999

SEASONAL TO INTERANNUAL VARIABILITY IN ANTARCTIC SEA-ICE SURFACE MELT

Mark R. Drinkwater and Xiang Liu
Jet Propulsion Laboratory
California Institute of Technology
4800 Oak Grove Drive, Pasadena, CA 91109

Abstract

Satellite remote sensing time series images are used to illustrate the spatial and temporal variability in Antarctic-wide ice-surface melting during the austral summer. Combinations of simultaneous data from the Active Microwave Instrument on board the ERS-1/2 spacecraft, RadarSat Synthetic Aperture Radar (SAR) and SSM/I passive microwave radiometer are employed in characterization of the effects of surface melting on measured values of the normalized backscattering cross-section, and brightness temperature, respectively. Time series from ERS-1/2 and the NASA Scatterometer are primarily employed to illustrate the typical progression of atmospherically-led surface melting and to demonstrate the similarity of spatial patterns observed in C-and Ku-band images. An algorithm is developed on the basis of the observed signatures which is used to map the interannual variation in the onset of summer season melt between 1992 and 1997. The algorithm is further adapted to record the cumulative number of melt days throughout the austral summer melt period. Results indicate that sea-ice surface melting is sparse and relatively short-lived, in contrast to the protracted Arctic summer melt season. Furthermore, regions consistently experiencing melt periods of 15 days or longer duration are focused around the Antarctic Peninsula, primarily in the north-west Weddell and Bellingshausen Seas. In 1995, melting lead to widespread regional melt-ponding, observed *in-situ* for the first time in Antarctica. Other years indicate similar characteristic melt patterns, perhaps in response to regional warming which has taken place in the Antarctic peninsula region. Results signal that Antarctic sea ice is close to a critical threshold with respect to the number of cumulative melt days. Initiation of the albedo feedback mechanism would lead to accelerated summer surface ice decay more typical of the Arctic basin.

Keywords

Sea ice, Antarctic, melt, microwave, radar, radiometer, ERS, NSCAT, SSM/I, scatterometer, SAR, seasonal, interannual, melt pond, austral summer.

1. INTRODUCTION

Fundamental differences exist between Antarctic and Arctic sea-ice with respect to its spatial and temporal variability in response to seasonal atmospheric and oceanographic forcing. In summer, the Arctic Ocean basin remains populated by old, multiyear ice, surviving each melt season by way of its thickness, to subsequently thicken under autumn cooling and winter growth. Antarctica, however, has no widespread multiyear ice counterpart, and for the most part non-landfast sea ice experiences only one summer melt period before drifting into high oceanic heat-flux regimes and melting. Sea-ice dynamics regulate the maximum age of the ice cover, particularly in the Weddell and Ross Seas, where cyclonic ocean gyre circulations sweep sea ice northwards. The relative age and thickness of the residual autumn ice cover maintained in these gyres is a critical variable to the stability of the upper ocean in and around Antarctica. Summer sea-ice melt helps to freshen and stabilize the mixed layer, thereby providing a thermal barrier to warming from beneath (Martinson and Iannuzzi, 1998). Furthermore, insulation afforded by a snow cover, found on summer sea-ice, prevents complete seasonal removal of the seasonal ice cover.

Around Antarctica, summer air temperatures rise only sporadically above 0°C. Consequently, classical surface melt-ponding has rarely been observed on field experiments and the sea-ice surface typically retains a snow cover year-round. Conversely, Arctic summer surface melting results in the expression of melt ponds over up to 60% of the surface as the snow cover disappears completely. Meltwater infiltrates the warm, porous sea ice, flushing out its salt content to leave it relatively brine-free. The fact that the Antarctic snow cover is retained throughout summer helps to insulate the ice, to maintain a relatively higher mean salinity in thicker ice, and to protect the sea ice from temporarily warm air temperatures (Andreas and Ackley, 1982).

This paper addresses the question of "what role surface melting plays in the retreat of the Antarctic sea-ice cover during the summer months." In this context, satellite microwave remote sensing data are used to measure the timing of the onset of melting and the extent and duration of the melt season. The primary data set was generated from two series of wind scatterometer backscatter measurements spanning several years. With continuous night and day operation, coupled with the all-weather imaging capability, scatterometer images have been demonstrated to provide an

effective method of monitoring the seasonal characteristics of the global sea-ice cover (Drinkwater Long and Early, 1993; Long and Drinkwater, 1999). No such other global radar data set presently exists, nor is there other suitable proxy climate data available which would help characterize the spatial and temporal variability of Antarctic surface melting.

2 BACKGROUND

The first *in-situ* field observations of Antarctic austral summer sea-ice surface melt were made in the Bellingshausen Sea by Arctowski (1908) on Belgica in 1899, and later by Wordie (1921) during the ill-fated drift of Endurance in the Weddell Sea from 1914-1916. It has been 100 years since these pioneering ship drift experiments, yet little more is known about the spatial extent, duration, frequency of seasonal surface melting of sea ice during the austral summer, or indeed its interannual variability. Both experimenters independently reported that Antarctic sea ice does not experience widespread vigorous summer surface melting, as is characterized by the formation of extensive ponding at melt maximum in the Arctic (Gogineni *et al.*, 1992). Despite surrounded by relatively warm ocean surface waters, some energy balance studies have suggested that the resulting combined surface radiative and turbulent heat fluxes are insufficient to induce widespread, protracted surface melting (Andreas and Ackley, 1982). The appearance of surface melting on sea ice is particularly important since it modifies the albedo of the surface of the ice and thus has a large impact on the radiative component of the surface energy balance during summer. With a winter to summer retreat in areal extent of the Southern Ocean sea-ice cover from 20×10^6 to 3×10^6 km², observed by SSM/I (Gloersen *et al.*, 1992) and Scatterometer (Long and Drinkwater, 1999), the Antarctic sea-ice cover has a significant impact on the net albedo of the Southern Hemisphere.

The so-called "albedo-feedback" effect (Curry *et al.*, 1995) results in Arctic melt ponding and ultimate removal of a large fraction of sea-ice during the summer months. This feedback operates when snow surface melting reduces the mean spectral albedo of the surface from ~0.9 to 0.7 or less (via thermal alteration of snow grains and reduced reflectivity, and appearance of water in liquid phase) (Maykut, 1985). Increased absorption of short-wave and trapped long-wave radiation results

in larger amounts of energy expended in melting of the snow and sea-ice surface and a further reduction in the spectral albedo. This positive feedback causes a vicious cycle which accelerates the removal of large expanses of Arctic ice too thin to survive an extended summer period of combined surface, lateral and bottom melt. In Antarctica, sea ice is completely surrounded at lower latitudes by ocean. Intuitively, therefore, summer storms are expected to be capable of delivering significant quantities of heat to the austral summer ice pack. Yet large regions of sea ice manage to survive the austral summer in spite of this and the relatively high ocean heat flux environment (McPhee and Martinson, 1994; Martinson and Iannuzzi, 1998).

Previous work using microwave radar data have characterized Arctic summer ice melt at a variety of frequencies (Carsey, 1985; Drinkwater and Carsey, 1991; Gogineni *et al.*, 1992; and Winebrenner *et al.*, 1994). Based upon these observations, Winebrenner *et al.*, (1998) recently reviewed observations of melting in Arctic satellite radar data. Primarily, previous research dedicated to automated recognition of the expression of melting in radar data have focused specifically on the summer decrease in perennial ice backscatter which is evident in Arctic high resolution SAR data. Since the observations summer melting by Carsey (1980) and Drinkwater and Carsey (1991), no attempts have been made to exploit scatterometer data for this purpose. In their summary of the state-of-art Winebrenner *et al.* (1998) concluded that "much work on automated recognition and mapping of seasonal transitions on sea-ice remains to be done."

It was the objective of this work, therefore, to develop a methodology for exploiting the long-term scatterometer microwave image time series for deriving melt information. The primary criteria were (i) that the derived products must be of practical value to the current generation of General Circulation Models (GCMs), and (ii) that they contain sufficient spatial and temporal information with which to interpret the seasonal progression of melting and the duration of melt season. Importantly, the resulting gridded data products must be applicable to prescribing seasonal changes in the albedo boundary conditions presently used in GCMs. Without such information it is impossible to correctly predict the response of the climate system to these sea-ice feedbacks.

The following sections describe first the satellite, *in-situ*, and meteorological data sets which were used in the study. Second, an error modeling study is undertaken to quantify the effects and impact

of wind speed variability during low summer ice concentrations. Third, a description of the algorithm and methods employed in melt detection are provided. Fourth, results of measuring the seasonal and interannual variations in surface melting are discussed, together with the conclusions of this study.

3. DATA SETS

Both active and passive satellite microwave remote sensing data were used in this melt study together with *in-situ* field measurements and meteorological data. Data were collected through a number of carefully coordinated, simultaneous field and satellite data acquisitions between 1992 and 1997. As the most suitable overlapping *in-situ* and remote sensing data sets exist for the Weddell Sea, we restrict our description of direct surface observations of melting to this region. Figure 1 shows the area of focus in the north-west Weddell Sea where a variety of data samples were selected to provide radar and radiometer characterizations of surface melting.

3.1 Satellite Data

The following sections describe the satellite data sets used to study surface melt.

Wind Scatterometer

The ERS wind scatterometer (EScat) is a sub-system of the active microwave instrument (AMI) flown on the ERS-1 and 2 series of satellites from 1991 until the present day. This instrument measures VV-polarized, C-band (5.3 GHz) normalized backscatter (σ^0) along a single 500 km-wide swath, with an absolute accuracy of 0.2 dB (Attema and Lecomte, 1998; Lecomte and Wagner, 1998). On August 16, 1996, the NASA scatterometer (NSCAT) was launched. In contrast to EScat, it measured Ku-band (13.995 GHz) backscatter at VV and HH polarizations along a 600 km-wide swaths on either side of the satellite. The σ^0 computation error has been estimated at less than 0.1dB (Tsai *et al.*, 1998). Unfortunately, due to failure of the ADEOS platform, data were only acquired until June, 1997. Both ESCAT and NSCAT swath measurements were been processed using the scatterometer image-reconstruction with filtering (SIRF) algorithm (Early and Long, In

Press). Enhanced resolution image data were produced with a 6-day temporal window, and resampled onto a polar stereographic grid. The final products comprise Antarctic 6-day mean images at 3-day intervals having a pixel spacing of 8.8 km and 4 km, for ESCAT and NSCAT respectively. Images span the period from 1992 through the present day.

Time series were derived of the mean 40° incidence-angle-normalized backscatter coefficient, $\sigma^\circ(40^\circ)$ (hereafter A) from each of the numbered boxes in Figure 1. These data are used to illustrate the seasonal and interannual variability of sea ice in the north-western Weddell Sea and to characterize the typical backscatter transitions taking place as the ice undergoes seasonal surface melt. Later, the image data are exploited to extrapolate these regional melt characteristics in an Antarctic-wide melt detection algorithm.

Synthetic Aperture Radar

High-resolution synthetic aperture radar (SAR) snapshot images are also used in this study to identify ice-surface characteristics, to evaluate open-water wind conditions, and to make estimates of local ice concentration. Summer ERS-1 data acquisitions from February and March 1992 have previously been analyzed and published in Drinkwater and Lytle (1996). These data were collected during the drift of Ice Station Weddell (Gordon *et al.*, 1993) and illustrate the end of the summer melt and freeze-up transition period in 1992 (see Figure 2). Further pairs of overlapping, ascending and descending ERS-1 SAR orbit data were acquired on 11th and 14th February (shown in Figure 1 and Figure 4a), and 12th and 15th February, 1995, each spanning several hundred kilometer long swaths. Figure 1 shows two descending ERS-1 SAR mosaics (dashed) from 11th and 14th February on a polar stereographic grid projection. These crossed the open ocean limit of the marginal ice zone (MIZ) at around 65° S into high concentration ($> 95\%$) perennial ice south of 67° S (Figure 3a).

Additional RADARSAT ScanSAR images were acquired on 19th, 22nd, and 28th December, 1996. The location of the wide-swath mosaic from orbit 05994 on 28th Dec is shown in Figure 1. Together with the ERS-1 SAR images and EScat data, these RADARSAT images ensure that *in-situ* and remote sensing examples are available from the summers 1991/92, 1994/95, and 1995/96.

SSM/I

Passive microwave data were acquired by the Special Sensor Microwave/Imager (SSM/I) series of instruments flown on the Defense Meteorological Satellite Program (DMSP) satellite series from June 1987 through the present day. The primary sensor products used in this study are gridded 19.4 and 37 GHz v-pol brightness temperature image data obtained from the National Snow and Ice Data Center (NSIDC). Corresponding daily, polar stereographic gridded sea-ice concentration data (Cavalieri, 1984) were also obtained at a pixel spacing of 25 km. For comparison, we reprocessed the data into 6-day average images at 3-day intervals in a similar manner to EScat images.

3.2 Meteorological Data

Meteorological data are useful to interpreting the microwave data and to understand the ice surface melting mechanisms. Daily heat flux and air temperature data were extracted from the NCEP/NCAR reanalysis data for the corresponding period 1992 - 1997. These data are gridded product on a NCEP's Gaussian grid, with a zonal 1.875° interval and a varying meridional interval of around 1.9° in the region shown in Figure 1. Data were extracted from grid points corresponding closest to the regions of interest, and averaged with a 6-day moving window at a sampling interval of 3 days.

Meteorological data recorded by various local Antarctic peninsula stations and an automatic weather station (AWS) were acquired for the purposes of comparison with the image data and validation of the timing of melt onset (identified by labeled triangles in Figure 1). Air temperature datasets for (a) Marambio (M) from Jan. 1 1988 to Dec. 31 1997; (b) Faraday (F) from Jan. 1 1986 to Dec. 31 1995; and (c) the Larsen Ice Shelf AWS (L) from Jan. 1 1986 to Nov. 30 1995 are shown in Figure 2.

3.3 In-situ Data

Field measurements were made during the drift of Ice Station Weddell (Gordon *et al.*, 1993) during the period from February until June, 1992. Although this coincided with the early part of the 3-day ice-orbit phase of the ERS-1 time series, *in-situ* measurements were made between February and

March which were coincident with both SAR and EScat data. Results of these observations are described in greater detail in Drinkwater and Lytle (1992).

Further field measurements were acquired between 10-15 February, 1995 from H.M.S. *Endurance* (Low, 1995). The British Royal Navy icebreaker positioned herself to collect simultaneous *in-situ* data during the ERS-1 overpasses described in the previous section. One helicopter facilitated surface data collection while another was equipped for aerial photography. The 11th and 14th February descending pair of SAR swaths were acquired during daylight (09:25hrs local time), thereby enabling detailed air-photo comparisons (Drinkwater *et al.*, 1998a; 1998b).

4. ENVIRONMENTAL CONDITIONS

4.1 Seasonal Air Temperatures

Meteorological time series data from the peninsula stations in Figure 2 show the typical seasonal cycle in air temperatures. Marambio and the Larsen AWS indicate air temperatures rising from early October, typically through mid-November before the first appearance of positive values. Air temperatures typically quickly fall again during the months of February or March. The onset of the freeze-up varies considerably, with significant interannual variation, depending on the duration of the summer melt period.

On the western side of the Antarctic peninsula, Faraday typically experiences warmer and longer summers and less intense winters than those on the eastern side of the peninsula in the Weddell Sea. Marambio, which has the most consistent long-term record, shows brief periods with summer air temperatures exceeding zero degrees, and longer spells of positive or melting degree days in 1993 and 1995. The Larsen AWS consistently experienced problems with calibration of air temperatures during the summer months. Nevertheless, the Larsen AWS helps to define the seasonal cycle in temperatures, particularly in 1995 when the *Endurance* field data were obtained. In these data the freeze-up occurs dramatically with air temperatures dropping below -10°C towards the end of February. The north-south seasonal air temperature gradient along the Antarctic

peninsula is also clearly evident, with typically 10°C difference between Marambio and Larsen in the period March through September.

4.2 Summer Ice Conditions

Summer ice conditions typical of the north west Weddell Sea are described by two SAR mosaics in Figure 3a and 3b. In February 1995 (Figure 3a) the mosaic shows an embayment in the ice margin with the outermost edge aligned east west at around 65° South. Box 15 (in Figure 3a) remained partially covered by sea ice of low concentration (< 50%) up until freeze-up, due to a northward coastal extension in the ice edge (dashed line) off James Ross Island. This extension in the ice margin was delineated in the ascending orbit ERS-1 SAR mosaic obtained on 12th and 15th February, 1995). Helicopter transects and aerial photographs along the white lines in Figure 3a (from Low, 1993) indicate ice concentrations rapidly increased to over 85% within ~75 km of the ice edge. Sea ice south of 66°S latitude (such as box 13) had concentrations exceeding this value.

Surface melt is demonstrated to have a significant effect upon regional signatures in the north western Weddell Sea. *In-situ* observations of melting made in February 1995 explain the widespread reduction in A values in box 7, 8, 15, and 16. Figure 3c shows a 10 km vignette of an ERS-1 SAR scene obtained coincident to aerial photographs made from Endurance (centered on white spots). The photograph from the highlighted black box indicates the lower left edge of the large floe, approximately 6 x 7.5 km in size, situated 100 km inside the ice edge at 65.85°S 55.75°W. Large melt ponds (up to 50m across) are evident on the large floe. Until this experiment, such melt ponds had never before been observed in the Antarctic. Similar ponding is also observed on smaller ice floes (15-200m in diameter) seawards to within 2-3 km of the ice edge before floes became too small to support surface ponds. Measurements also indicated that such perennial floes were typically 2.5-4m thick with a 2-15 cm deep snow cover.

The melt ponds themselves do not appear to have a significant enough response at 23° incidence that they stand out in the high-resolution, SAR image. Nonetheless, due to the melt pond areal coverage in the photograph it is apparent that the average calibrated ice-floe backscatter coefficient is depressed from cold, winter values typical of old ice (Drinkwater, 1998). By the same token

regional ice signatures in low-resolution, higher incidence-angle EScat data are expected to reflect this depression of typical sea-ice backscatter values as a function of how widespread surface melting is.

Figure 3b shows contrasting ice conditions at the end of December 1996, with a distinctive coastal polynya and lower concentrations along the coast. Although box 15 lies off the top edge of the mosaic, the SAR orbit acquired several days earlier indicates typical marginal ice zone conditions and an ice concentration of around 15% in this northernmost sample box. The central sea-ice region around box 16 has an ice concentration of around 50%, while further to the south box 13 has a concentration exceeding 95%. In Figure 1, and to the lower left side of Figure 3b, box 1 indicates a control sample box on what was originally the northernmost piece of the Larsen Ice Shelf (LIS) or Larsen A (Rott *et al.*, 1996). LISa disintegrated in 1992 and subsequently fast ice formed which remained in place until the end of December, 1995. The image in Figure 3b successfully captures the break out of this fast ice in response to the seasonal melt and a likely combination of tidal flexure and swell from the north east. Box 1 was chosen because the time series data are effective in defining the melt period expressed on thick snow-covered sea ice. Furthermore, this sample region is close to Marambio, from which the air temperature record is plotted in Figure 2.

Figure 3b indicates the expression of melting on the Larsen B portion of the ice shelf (lower left image) as dark pixels. Further offshore, dark sea-ice floes surrounded by brighter material also confirm the expression of surface melting, particularly at the right (southernmost) end of Figure 3b. Long and Drinkwater (1999) previously showed time series EScat and NSCAT images which illustrate the progression of seasonal ice shelf melting and its interannual variability. Local ice shelf melting is particularly important as a means of confirming the effects of regional air temperatures along the peninsula.

5. REGIONAL SCATTEROMETER SIGNATURES

When interpreting the seasonal variations in EScat backscatter time series derived from the sample boxes in Figure 1, it is important to be able to quantify the effects of ice concentration, fluctuating

wind speed, and thermal cycling. Each may have an impact upon the regional mean backscatter measured by a scatterometer instrument.

5.1 Impact of Air Temperature

Previous work by Drinkwater and Lytle (1997) showed that at ice concentrations exceeding 95%, the modulation of the regional backscattering coefficient by wind speed and direction was negligible. They investigated the relationship between the EScat A values, high-resolution SAR backscatter coefficient measurements of sea-ice, and *in-situ* wind and air temperature conditions measured at Ice Station Weddell (at around 72°S, 53°W). No correlation was observed between the satellite-measured backscattering coefficients and wind, implying that the fetch-limited, wind-induced roughening effect on small leads was insufficient to cause significant bias in regional mean A values. The observed variability in SAR backscatter and EScat A values was instead highly correlated with air temperatures measured by the meteorological station at Ice Station Weddell and buoys surrounding the ice camp (Drinkwater and Lytle, 1996). Furthermore, *in-situ* measurements by thermistors embedded within the sea ice showed that the thermal gradient within the snow and sea ice determines the magnitude of the snow-ice interface reflection coefficient. In this manner, seasonal air temperatures regulate the regional backscatter of the summer sea-ice pack.

5.2 Modeling of Wind Impact

At relatively lower ice concentrations (< 90%) the wind can have a non-negligible contribution to the regional averaged A values. Here we use a simple model to demonstrate the effects of wind on the weighted mean backscatter coefficient at varying concentrations of typical perennial and seasonal sea ice. The intention is to quantify wind effects in ice conditions more typical of the summer ice margin in Figure 3, where ice concentrations vary between 15 and 90 %, and where summer surface melting is experienced. The model is based on the following equation:

$$\sigma_{tot}^o = A_i \sigma_{ice}^o + (1 - A_i) \sigma_{ocean}^o \quad (1)$$

where A_i is fractional coverage of ice, σ_{ice}^0 is the regional mean sea-ice backscatter coefficient, σ_{ocean}^0 is the backscatter coefficient of the wind-roughened leads or open water fraction, and σ_{tot}^0 is the weighted mean regional backscatter coefficient. The value of σ_{ocean}^0 is computed using the CMOD4 transfer function, which characterizes the backscatter as a function of wind speed, incidence and azimuth angle (Stoffelen and Anderson, 1997). Model results in Figure 4 are computed for a fixed 40° incidence angle, to correspond with EScat A values. An azimuth angle of 0° (relative to the wind direction) is arbitrarily chosen, since the largest effective wind modulation of backscatter occurs when the viewing geometry is aligned downwind in the wave propagation direction. Two extreme cases are chosen, first in Figure 4a for varying concentrations of typical winter perennial ice (with relatively high backscatter coefficient) and second in Figure 4b for varying concentrations of melting perennial ice or seasonal ice (each with similar backscatter values).

Figure 4a shows the wind speed influence upon backscatter coefficient for typical winter perennial sea ice (where $\sigma_{ice}^0 = -8$ dB after Drinkwater, 1998). In the austral summer, typical wind speeds of 0 - 15 m/s are observed (Drinkwater and Lytle, 1997).. In this range, the modeled regional mean backscatter coefficient increases with ice concentration and tends to A values for 100% concentration sea ice. Higher ice fractions per unit area imply greater mean backscatter values, because in general large proportions of perennial ice have higher backscatter values than the remaining wind-roughened open water up to wind speeds of 17 m/s. For concentrations higher than 0.6, the backscatter varies within ± 2 dB. Backscatter values vary by a maximum of $\sim \pm 4$ dB for sea ice concentrations ranging from 0.4 to 1 over the entire wind speed range.

In contrast, for summer melt conditions in Figure 4b, or typical winter seasonal sea ice backscatter values (where $\sigma_{ice}^0 = -15$ dB), there is a larger increase of ~ 4 dB in modeled regional A values as wind speeds increase. At wind speeds below 7 ms^{-1} , regional mean backscatter values remain depressed below mean A values of the surrounding sea ice. However, the wind-speed threshold at which mean backscatter may be biased high is lower for seasonal or melting ice. High wind speeds ($> 15 \text{ ms}^{-1}$) can cause increases in the effective regional mean backscatter exceeding 5 dB at low ice concentrations (< 0.4). This is particularly important when considering surface melting in marginal ice zones with low summer concentrations (such as box 15 in Figure 3). Nevertheless,

since the impacts of limited fetch and stable boundary-layers are disregarded here, the modeled extrema in A may be considered upper bounds to the effect of wind upon EScat-observed values.

6. MELT DETECTION ALGORITHM

As stated in the previous sections, the effect of summer melt is observed as a spatial and temporally varying reduction in scatterometer A values. The spatial pattern of this reduction is expressed in two EScat A sub-images in Figure 5, in the north west Weddell Sea, in the vicinity of the Antarctic peninsula. Figure 5a indicates a mean 6-day image for the peak melt period in 1995, between 5 and 10 January. The color table values were optimized in Figure 5 to indicate the melt-front. Melting ice surfaces are observed to have values below -20 dB, at the boundary between light blue and dark green colors. The pattern of melting is relatively coherent, extending approximately east-west, with a finger of values below -25 dB extending the south-west onto the southern portion of the Larsen Ice Shelf. In some locations, the impact of surface melting upon the backscatter is patchy with a large 100 x 100 km isolated patch of perennial ice (beneath the descending SAR swath on 14 Feb, 1995) which until 10 February appears to have survived the effects of melting. As snow-depth has a large impact upon insulating the surface of the sea-ice (Massom *et al.*, 1997; Massom *et al.*, 1998), areas of large fractions of thick snow-covered perennial ice react slowest during brief periods of warming. This effect can be exaggerated by the layered snowcover found on perennial sea-ice floes in the Weddell Sea (Drinkwater and Haas, 1994). Deep, low thermal conductivity snow can support a strong negative temperature gradient (Massom *et al.*, 1998), which can effectively conduct heat away from the snow/air boundary under brief periods of downward heat fluxes.

Figure 5b indicates the period of simultaneous SAR and *in-situ* measurements from HMS *Endurance*. By 14 February the residual patch of perennial ice sampled *in-situ* by helicopter, had begun to melt, with a reduction in regional A values of ~8 dB. According to observations in Figure 3c, and confirmed by the box 13 time series, the appearance of surface melting and of extensive melt-ponding resulted in the reduction of typical perennial ice A values (~ -8dB) to values below -16dB. Meanwhile, the general northward movement of the melt front in other areas indicates that the southernmost air temperatures are slowly cooling. Larsen ice shelf A values in the vicinity of

the Larsen AWS are observed to have increased by over 10 dB, while cooling of perennial sea-ice areas to the south of Marambio restores local signatures back to their former A values.

Figure 6 shows a temporal zoom of the 1994-95 melt transition in box 15 (in Figure 1). The melt onset is characterized by an abrupt decline in backscatter of several decibels over a contiguous time period exceeding a week. This decline occurred at a time when the ice margin was far north of this box location and ice concentration was at its highest. In 1994/95 a reduction in backscatter of 7 dB occurred over a period of 21 days (or seven images spaced at intervals of 3 days) in the region observed to be melting in Figure 3a. The accompanying plot of $\delta A/\delta t$ in Figure 6b indicates that the time derivative of A remains negative for a period of 8 consecutive images, or 24 days. The combination of these two criteria has the advantage of filtering out small rapid fluctuations occurring as a result of the combination of oscillating spring air temperatures, variable ice concentrations and mid-winter storms.

Winebrenner *et al.* (1994, 1998) illustrated machine-automated algorithms for retrospective estimation of melt onset dates within geographical cells using low-resolution (100m) ERS-1 SAR imagery for the Arctic. Here, an equivalent melt-detection algorithm was developed to detect the onset of melting and the number of cumulative melting days for EScat and NSCAT scatterometer images of Antarctic ice. For easy comparison, higher resolution NSCAT data were resampled into the same grid as EScat. A 15 x 15 pixel two-dimensional spatial Gaussian filter ($\sim 132 \times 132$ km) was first applied to the images to reduce orbit swath noise. Noise is manifested particularly in EScat data of the Weddell and Ross Seas as a result of large spatial and temporal variability in sampling due to conflicting SAR operation of the ERS-1/2 AMI instrument within direct broadcast range of the O'Higgins (see Figure 1) and McMurdo SAR receiving stations.

For this study, data processing was limited to pixels in the EScat image between the sea-ice margin (determined by the SSM/I-derived 15% ice-concentration contour) and the Antarctic coastal mask. The backscatter change between two consecutive images was iteratively computed at each pixel location and stored. At each time step temporal pixel differences were computed and stored in memory for 7 contiguous floating point images (spanning an 18 day period for EScat and NSCAT data), requiring approximately 60 mB dynamic memory. For each pixel, the melt onset date was

determined when the following criteria were met. In the case of Antarctic sea ice, the A value decrease from one image to the next must exceed 0.5 dB, and the total decrease within the 7 consecutive images window was no less than -3 dB. After each sea ice pixel was searched and checked for melting, the array is shifted to the next image, another set of 7 consecutive images is loaded and the process repeated.

To test and validate the approach, the algorithm was applied to a series of examples. Firstly the melt-detection criteria were applied to the time series at the location 64°S 56°W in Figure 6. The algorithm automatically selected day 319 (or 15 November) of 1994 as the date of melt onset. Figure 2 suggests that this date coincides with air temperatures increasing and remaining for the first time consistently above -5°C at the Marambio coastal station.

To further validate the expression of melt onset in the regional sea-ice signatures of the north-west Weddell Sea we selected time series first from the control boxes shown on the nearby Larsen ice shelf (LIS). Ice shelf signatures offer the advantages of ruling out the possibility effects due to ice concentration variability or advection of varying sea-ice types (with different backscatter) through the fixed sample regions. Figure 7 shows the results of plotting a blow-up of the 1996/97 melt season for LIS boxes (numbered 1-4), together with contrasting time series from sea-ice boxes 15 and 20. The upper panel indicates a large dynamic range in A values as a result of austral summer melt as far south as 68° S. Decreases of 10 to 20 dB occur relative to the stable winter values, and melting is confirmed by concurrent SSM/I 19 GHz v-polarized T_b values tending to 273 K (Drinkwater *et al.*, 1998a; Long and Drinkwater, 1999). Figure 7a indicates the sharp definition of the melt onset in boxes 1-4 as an initial 10 dB drop in A values. For comparison, the algorithm-retrieved melt onset is shown as a cross for each of the boxes. Moreover, the algorithm correctly recognizes identical onset dates in each of the time series despite the different mean backscatter values of ice-shelf and fast-ice regions. False identification of brief periods of melt (due to strong cyclonic activity prior to onset of summer season melting), such as that observed in northernmost boxes 1 and 2, was avoided by adjusting the temporal windowing method described above.

The lower part of Figure 7 shows accompanying information derived for boxes 15 and 20, together with the Marambio air temperature record and the accompanying NCEP latent heat fluxes. Just

prior to the detected onset of melt, air temperatures increased from -20°C to -2°C in the space of 2 weeks. At the same time, NCEP data indicate that the surface flux of latent heat reverses from typical mid-winter values of below -20 Wm^{-2} to become positive. This indicates that heating is supplied from the atmosphere to the surface to change snow from solid to liquid phase and to induce melting. This precursor to melt onset corresponds with the dip in A values observed at 1996.83 in Figure 7a in both box 1 and 2. As summer melt onset progresses, the mean NCEP latent heat flux tends to values close 0 Wm^{-2} . During this period typical air temperatures at Marambio remain fairly stationary at close to 0°C , and brief peaks of positive excursions in air temperatures are accompanied by peaks in the NCEP surface flux of latent heat. Box 15 (solid line in the upper panel of Figure 7b) responds to the melt precursor with a 3 dB dip in backscatter prior to the true onset of melt. Afterwards A values decline as a combination of the effects of seasonal melt and reductions in ice concentration to the values of $\sim 15\%$ evident in the 28 December SAR mosaic (in Figure 3b).

In contrast box 20 shows a different characteristic seasonal trend (Figure 7b) with a summer peak in A . This box is beyond the southernmost point of penetration of the NCEP seasonal 0°C isotherm in the western Weddell Sea. Drinkwater and Lytle (1996) found that a similar distinctive summer maximum in backscatter February 1992 was accompanied seawater flooding of the snow-ice interface of perennial snow-covered ice found in this region. Snow-covered perennial ice floes surrounding Ice Station Weddell (ISW) increased their σ_w values in austral summer as a result of ice-surface flooding at the base of the snow. Since air temperatures at this latitude are too cold for snow-surface melting, the snow must insulate the ice sufficiently for it to become warmer, by heat supplied from beneath. At temperatures beyond a threshold of approximately -8°C (Crocker and Wadhams, 1989) the ice becomes permeable. If the snow cover is deep enough for an isostatic imbalance (Massom *et al.*, 1997) then it may flood with seawater through open brine drainage channels, causing the widespread increase in σ_w plotted by Drinkwater *et al.* (1998a).

In-situ data from ISW in 1992 confirms that summer increases in A values are not caused by atmospherically-led surface melting. Box 20 results in Figure 7b and other such sample boxes in Figure 1 are disregarded as experiencing melting. Further support for this assumption is provided in Figure 4b, which confirms that low ice concentrations and sustained high wind speeds would be

necessary throughout the summer months to be able to effect the observed increase in Figure 7b from -15 to -10dB. Importantly, seasonal increases in backscatter are consistently observed in each of the sample time series south of box 9 (i.e. boxes 10, 11, 12, 18, 19, and 20), implying that the effects of surface melting rarely penetrate south of 67° S on the sea ice. Though this is contrary to box 3 and 4 ice-shelf observations of melting in Figure 7a, patterns of low backscatter values in EScat images clearly show localized regions of surface melting fringing the Antarctic peninsula, rather than extending out into the Weddell Sea.

7. RESULTS

7.1 Melt Onset Patterns from ESCAT and NSCAT

The melt algorithm was first applied to map the spatial pattern of seasonal melt onset for the entire image time series between 1992 and 1997. To check the consistency of melt onset retrieval between frequencies and instruments we first compared results from simultaneous ESCAT and NSCAT observations. Figure 8 shows a comparison of results from each instrument for the austral summer of 1996-97. A color bar and legend indicate the day of year on which melting began. Blues and greens represent melt onset during November and December, while browns, reds, oranges and yellows highlight successively later melt onset during January, February or March, respectively. The SSM/I-derived 15% ice concentration contour is indicated for day 313 (8 November, 1996) to delineate the outer ice margin at the beginning of ice-edge recession, prior to melt onset on day 319 (also shown in Figure 7a as crosses). An inner line delineates the 15% ice concentration contour at the end of the algorithm run (day 73, 14 March, 1997).

Figure 8 indicates that the frequency difference between Ku-band NSCAT and C-band EScat has little impact upon the detection of melt onset, and that the melt process effects a similar spatial response at both wavelengths. The algorithm is relatively robust, sensing regionally consistent dates of melt onset throughout the ice cover. The primary difference is that Ku-band data have a higher resolution and capture a larger dynamic range, and thus are more sensitive to the appearance of melting signatures. This sensitivity leads to more successful NSCAT recognition of melting in parts of the central Ross Sea, particularly in locations experiencing only brief bouts of surface melt, or

mixed pixel effects. Though there is a difference in sensitivity to melting, the detection criteria used for the NSCAT result in Figure 8b are more stringent than with the EScat data. Melt criteria used for the EScat data were relaxed to most closely resemble the results obtained with the higher resolution NSCAT data.

To validate the spatial patterns we have compared the time-tagged colored patches in Figure 8 (indicating contiguous regions of detected melt onset) with gridded NCEP data (described in section 3.2). NCEP reanalysis products were used exclusively in the peninsula region, as these data are expected to have the largest number of station meteorological data assimilated into the products. Figure 9a and 9b shows contoured fields of the surface flux of latent heat, and corresponding air temperature, for the first detected onset of melt on day 319, 1996. NCEP data indicate, as described in the previous section, that warm air temperatures and positive latent heat fluxes during early summer are confined to the westernmost portion of the Weddell Sea. The location of the enclosed contour containing positive values exceeding 0 W/m^2 corresponds closely with the patch of day 319 melt onset on the east and west side of the Antarctic peninsula.

Andreas and Ackley (1982) previously demonstrated that for melting to occur in Antarctica, surface layer temperatures must be substantially higher than in the Arctic. This condition is true because the air is typically drier under the influence of dry continental winds (Schwerdfeger, 1970). Under typical springtime relative humidities of ~80%, the surface can tolerate higher temperatures without melting provided that advective heat loss by sublimation balances the large net radiation input at the surface. For melting to occur the surface layer temperature must be substantially higher than in the Arctic, and at or above 0°C for the typical Bowen ratios (i.e. the ratio of sensible to latent heat flux), wind speeds and humidities observed *in-situ*. Clearly it is rare for summer melting to occur with a negative latent heat flux, and only near the ice margin is there a source of warm, moisture-laden air which can induce melting. The NCEP data appear to indicate that the general conditions required are therefore a combination of large positive radiation balance, and a combination of both positive sensible and latent turbulent heat fluxes (i.e. from the atmosphere to the surface).

7.2 Seasonal Pattern of Melt Onset

Melt onset dates in Figure 8 indicate a poleward propagating melt front, moving progressively southwards with the seasonal air temperature increase. Surface melting is clearly not widespread nor is spatially contiguous at any given instant of time during the summer. Locations of melt patches appear linked to the locations of storm tracks supplying warm air masses and sufficient heat to induce only temporary surface melting. The pre-melt ice margin location and the ice margin, corresponding with the end of the melt transition period, indicate the distance of sea-ice margin recession during the melt season. It is apparent that large portions of the ice cover experience little or no surface melt during ice recession, suggesting that the atmosphere plays only a small role in removing sea ice from these regions in summer. Alternatively, though the ice margin in the north western Weddell Sea is replenished by ice drifting from the south, and despite early onset of melting shows only a minimal amount of recession.

Various isolated locations report melt onset, though obviously too far south to experience surface wetting as a result of snow melt. Indications of melt onset are observed late in the season in the southern Weddell Sea, and in particular along the Ronne-Filchner ice shelf front. In these locations thin high salinity ice forms in ice-shelf polynyas, and it is possible that air temperatures are elevated enough that surface warming causes brine volume increases and significant permittivity changes. The result would be a summer decline in thin ice signatures which simulates the effect of surface melting, particularly on newly formed expanses of thin ice without an insulating snow cover.

7.3 Spatial Pattern in Cumulative Melt Days

The cumulative number of days of summer surface melt are recorded by the algorithm for a given pixel from the melt onset date forwards. Since fluctuations in A values are common, periods of positive time derivatives (i.e. inferred cooling), such as in Figure 6b, are rejected. Figure 10 shows comparative results for the number of cumulative melt days recorded in each scatterometer data set. Notably, in order to obtain similar results for C- and Ku-band frequencies, the melt criteria had to be relaxed for ESCAT data (from -3 to -1 dB drop). This is partially attributable to increased

noise, reduced resolution, and lower sensitivity of the C-band A values to the appearance of moisture in the snow (*i.e.* reduced dynamic range).

Protracted summer surface melting in a specific region is rare and more likely to be short-lived. Instead of long periods with depressed backscatter coefficients, the summer is characterized by large fluctuations in backscatter indicating melting and freezing cycles (Drinkwater *et al.*, 1998). This behavior is not unique to the sea ice, but is also observed on neighbouring ice shelves, where meteorological station data (Figure 2) confirm the such temperature fluctuations.

The total cumulative melt days recorded by both instruments over sea ice confirm that austral summer melting is short-lived, patchy and ephemeral. The only sea-ice locations experiencing protracted vigorous melting (exceeding 30 days) in 1996-97 were regions bordering the Antarctic peninsula, in the Weddell and Bellingshausen Seas, and East Antarctic coastal regions. The southernmost melting region is observed in the Ross Sea, while an anomalous point location located in the Amundsen Sea (with values exceeding 20 days) is discovered to correspond with the location of the large, drifting Thwaites iceberg (A10).

7.4 Characteristics of the Annual Cycle

Time series microwave signatures extracted from sea-ice boxes in Figure 1 show variability indicative of seasonal and interannual changes in the characteristics of the snow and ice floe surfaces together with the proportions of ice types advected through each region. Figure 11 shows the results from two boxes of different sizes, and distances from the Antarctic peninsula. In each plot the upper panel shows the A values together with dotted lines indicating $\pm 1\sigma$ bounds computed from the statistics of each sample region in A images. Generally speaking, the larger the box, the greater the variance in ice conditions and backscatter, and box 9 in Figure 11a indicates slightly larger variance than box 22 in Figure 11b. The middle panel of each plot indicates the 5-year mean annual (dotted line) and filtered cycle (solid line), and the anomaly cycle in the lower panel shows the residuals after removing the smoothed 5-year mean.

The two examples indicate differences in the mean annual cycle as a consequence of the varying impact of melting, combined with the advection of varying fractions of seasonal or perennial ice through each box. Figure 11a shows a characteristic dip in October as summer approaches, and as the concentration of perennial ice dwindles as it is advected northwards out of the western Weddell Sea. The anomaly time series indicates that melting had a large impact on the summer signatures in 1992/93, 1994/95, and 1996/97, and summer oscillations in A in these time series indicate melt/freeze cycling. In the intervening years (1992, 1994, and 1995), a strong February-March peak in A indicates that larger than normal quantities of perennial ice were advected through the region. Corroborative field evidence was collected during the WWGS 92 shipborne field experiment, for instance, when swarms of large floes of thick perennial ice with > 1 m deep snow, were observed exiting the western Weddell Sea (Drinkwater and Haas, 1992).

The time series from box 22 shows a large contrast to box 9. It was selected because it experiences only brief periods of summer melting and is covered by high concentrations of sea ice throughout the period shown. This box is too far to the east to experience varying mixtures of perennial and seasonal sea ice, and this reflected in the lack of a consistent pattern to the seasonal cycle. The long-term mean backscatter value reflected by the stable mean annual value of -14.5dB in the central panel of Figure 11b is typical of deformed first-year ice (Drinkwater, 1998). Because of the flat-line characteristic of its annual cycle, box 22 serves as a unique indicator of small dynamic anomalies in this part of the Weddell Sea, as well as highlighting the anomalies resulting from periodic melt events such as occurred at the end of February in 1996.

7.5 Interannual Melt Patterns

Figures 11 and 12 compare the interannual variability in melt patterns deduced from the EScat data record, each having five panels indicating a single melt season. Figure 12 shows that most years generally exhibit a southward melt onset progression (from blue to red, to orange and then yellow). This results in early melt onset detection around the tip of the Antarctic peninsula (i.e. at the lowest latitude ice margin) and consistent melt extending eastwards along the sea-ice margin in the northern Weddell Sea, and westwards along the coast into the Bellingshausen Sea. Due to its simplicity, the current melting algorithm cannot differentiate if the melting is simply surface

melting or the ice has melted away completely. But by using ice edge information obtained from SSM/I, we can infer for instance that the melting in the Weddell Sea that occurs mostly at the end of January or early February is indeed surface melting.

More southern sea ice regions tend to experience later melt onset, as the sea-ice margin recedes southward. However, there is an exception to this rule, with early season melting consistently experienced in the Ross Sea. The melt onset algorithm also identifies isolated patches of late-season melt in the southern Weddell Sea (in February/March 1997). Though this ice is clearly not melting from above, such circumstances could occur in smooth, thin ice regions when ocean heat fluxes warm the ice significantly enough to increase the permittivity of the ice surface. The result would be to increase the reflectivity and to cause reductions in the A values, and possibly false melt onset detection.

Sea ice around East Antarctica demonstrates extremely rapid recession, with the result that melt onset is detected on the narrow annulus of remaining sea ice. In all years except 1993-94, coherent bands of similar melt onset may be traced around the ice margin in Figure 12. The cumulative melt days results shown in Figure 13 help to visualize the regions where seasonal melting has the largest impact. Consistent surface melting occurs between 30°E to 120°E, for about 15 days except for the anomaly of the 1993-94 summer. Some of this anomaly may result from a number of regions of missing data during the first half month of January in 1994 such that no cumulative melting was detected. However, that alone does not appear to explain some of the large differences in melt onset, for instance.

The cumulative melt summary demonstrates that although there is significant interannual variation in melting, there are a number of locations around Antarctica which experience a consistently large number of melt days (> 15) in a summer season. The results imply consistent summer melting around the Antarctic peninsula, with a more southern extension of melting on the western flank around into the Bellingshausen Sea. Coastal sea-ice regions of East Antarctica with the number cumulative melt days exceeding 15 are less frequent or extensive. In 1992/93 and 1996/97, extended melting is observed on the sea ice bordering the Amery and Shackleton ice shelves. The

Shackleton ice shelf in particular has been observed to have experienced considerable break up and calving over the last several years (Young, pers. comm.), perhaps in response to these melt events.

8. CONCLUSIONS

These results indicate that both ERS-1/2 (C-band) and NSCAT (Ku-band) scatterometer images can be used effectively to monitor the large-scale surface characteristics of austral summer ice in Antarctica. Since the value of radar backscatter coefficient at 40° is sensitive to changes in reflectivity, surface melting has a large impact on A values, which can be exploited in mapping surface melt. In May 1999 the QuikScat scatterometer will be launched. This instrument will have no conflict with SAR data acquisitions and will be used in developing a polar Ku-band time series to be employed in future 'routine' retrievals of sea-ice melt.

Application of the melt detection algorithm over the period 1992-98, spanning both the ERS-1 and -2 missions, provides valuable information about the interannual variability in surface melting on the Antarctic ice pack. For the first time, this provides insight into the contribution of the atmosphere to the austral summer ice retreat. Clear patterns exist in year-to-year atmospherically-induced surface melting, and NCEP surface fluxes indicate that the regions of melting correspond reasonably closely with regions with positive latent heat fluxes and air temperatures close to or above 0°C. In these cases, existing meteorological analysis data imply that heat delivered by the atmosphere is expended in surface melting, by the transformation of the snow cover on the sea ice from solid to liquid phase.

Annual trends in EScat σ^0 time series are explained primarily by a combination of seasonal changes in air temperature and advection of different ice types into/out of the study regions. Results indicate significant interannual variability occurs in the duration and intensity of the melt season, particularly in the north western Weddell Sea. The austral summers of 1992/93 and 1994/95 were relatively warm, each with earlier and more extended melt seasons. The 1995 appearance of melt ponding coincided with the rapid disintegration of northern sections of the LIS and landfast ice between James Ross Island and the peninsula (Rott *et al.*, 1996), and the calving of a spectacular

iceberg from LIS close to box 2. Though the February 1995 field observation of Antarctic melt ponds in 1995 coincided with these occurrences, it appears from the appearance of similar melt periods in other years that sea ice melt ponding may have been more widespread in the Antarctic peninsula region in recent years. Continuing warming presently occurring along the Antarctic peninsula is expected to have the most significant impact in this region by increasing the frequency of melt ponding, and ultimately leading to more significant changes in the location of the summer sea-ice margin. Although the current 1998/99 summer is not yet part of this melt data set, warming and consequent melt ponding is speculated as responsible for the extreme autumn April ice extent anomaly in the Bellingshausen Sea. The recent summer saw a rapid collapse of the Wilkins ice shelf front on the Western side of the Antarctic peninsula, also speculated to be linked to the warming trend in the peninsula region (Scambos, pers comm.).

Summer season surface processes have been shown to influence the microwave radar data in consistent and distinctive ways depending on whether the sea ice lies north or south of the seasonal isotherm corresponding to snow melting. Observation of summer increases in backscatter in many of the southern Weddell Sea sample boxes indicates the widespread nature of summer processes leading to upward meteoric ice growth, more commonly known as snow-ice (Drinkwater *et al.*, 1998a, Drinkwater and Lytle, 1997). Since most thermodynamic models do not adequately represent this process, our results are expected also to shed new light on the seasonality and regionality of this unique Antarctic summer upward-ice-growth process. Further studies will optimize the present algorithm to identify and track widespread increases in backscatter as a function of surface flooding events.

Antarctic sea-ice responds quite differently from its Arctic counterpart during the summer season. Atmospherically-led austral summer surface melting appears far less extensive in time or space than is experienced in the Arctic. This suggests that atmospherically-induced surface melting and resulting albedo feedback is not the dominant sea-ice removal mechanism in summer; but instead, that the oceanic heat flux and short-wave radiation absorbed by the ocean surface in small lead fractions is more effective in removing the summer sea ice cover. This implies that the retreat of the Antarctic summer ice margin is not simply regulated by the atmosphere, but rather by a balance between ocean heat flux, atmosphere, and sea-ice dynamics. Furthermore, the example of the

Thwaites iceberg drifting in the Amundsen Sea in 1996/97 provides an intriguing result. The iceberg's top surface apparently experienced over 15 more days melting than that experienced by the surrounding sea ice at sea-level, which would imply that there is a considerable temperature gradient in the lower atmosphere. Because of the typical strong and fairly ubiquitous summer Antarctic inversion, cold stable air close to the surface inhibits downward mixing of warmer air aloft. Icebergs, as well as standing higher in the inversion layer, induce downward mixing of warm air and appear more susceptible to summer surface melting. Future studies must focus on the general circulation patterns and atmospheric conditions in the boundary layer to clarify why large portions of the ice cover appear less susceptible than others to surface melting.

Future studies should develop an understanding of the relationship between summer melt and albedo changes as specific inputs to models. However, further work is first required to develop capability to use large-scale tracked ice kinematics products from scatterometer and SSM/I images in conjunction with these interannual time series. Dynamical information such as opening/closing will enable quantification of advective and dynamic influences upon the backscatter variability. On this basis, smart algorithms can be developed to more accurately extract thermodynamically-regulated sea-ice characteristics from such radar time series.

9. ACKNOWLEDGMENTS

ERS-1/2 SAR images were obtained through ESA Project AO1.PIP.ANT3 and Scatterometer data were delivered by IFREMER and analyzed as part of ESA Project AO2.USA.119. RADARSAT SAR data products were acquired from the Alaska SAR Facility through CSA/NASA ADRO Project 164, and SSM/I gridded data were kindly supplied by the National Snow and Ice Data Center. NCAR/NCEP are acknowledged for providing meteorological reanalysis data products, and the British Antarctic Survey for Antarctic weather station data. Doug Low is acknowledged for his important contribution to the analysis of the ERS Wind Scatterometer data. MRD and XL completed this work at Jet Propulsion Laboratory, California Institute of Technology under contract to the National Aeronautics and Space Administration. Funding was kindly provided by Dr. Prasad Gogineni of NASA Code YS (RTOP 621-21-02) and the JPL NSCAT Project Office.

10. REFERENCES

- Andreas, E. L., and Ackley, S. F., On the differences in Ablation Seasons of Arctic and Antarctic Sea Ice, *Journal Atmospheric Science*, 39, 440-447, 1982.
- Arctowski, H., Les Glaces: Glace de Mer et Banquises. Resultats du Voyage du S.Y. Belgica en 1897-1898-1899, *Rapports Scientifiques*, Vol. 5., J.E. Buschmann, Antwerp, [Trans., NTIS AD 881 363], 3-55, 1908.
- Attema, E.P.W., P. Lecomte: The ERS-1 and ERS-2 Wind Scatterometer, System Performance and Data Products, *Proc. IGARSS '98*, IEEE International Geoscience and Remote Sensing Symposium Proc., 4, 1967-1969, 1998.
- Carsey, F.D., Summer Arctic Sea Ice Character from Satellite Microwave Data, *J. Geophys. Res.*, 90, C3, 5015-5034, 1985.
- Cavalieri, D.J., P. Gloersen, and W.J. Campbell. Determination of sea ice parameters with the NIMBUS-7 SMMR, *J. Geophys. Res.*, 89(D4), 5355-5369, 1984.
- Crapolicchio, R., P. Lecomte: The ERS Wind Scatterometer Mission: routine monitoring activities and results, *Proc. of a Joint ESA-Eumetsat Workshop on Emerging Scatterometer Applications - From Research to Operations*, 5-7 October 1998, ESTEC, Noordwijk, The Netherlands (ESA SP-424, Nov. 1998), 285-298, 1998.
- Crocker, G.B., and P. Wadhams, Modelling Antarctic Fast Ice Growth, *J. Glaciology*, 35, 3-8, 1989.
- Curry, J.D., J.L. Schramm, E.E. Ebert, Sea Ice-Albedo Climate Feedback Mechanism, *J. Climate*, 8, 240-247, 1995.
- Drinkwater, M.R., Satellite Microwave Radar Observations of Antarctic Sea Ice. In C. Tsatsoulis and R. Kwok (Eds.), *Analysis of SAR Data of the Polar Oceans*, Chapt. 8, 145-187, Springer-Verlag, Berlin, 1998a.
- Drinkwater, M.R., Active Microwave Remote Sensing Observations of Weddell Sea Ice. In M.O. Jeffries (Ed.) *Antarctic Sea Ice: Physical Processes, Interactions and Variability*, Antarctic Research Series, Vol. 74, 187-212, American Geophysical Union, Washington, D.C., 1998b.
- Drinkwater, M.R., and F.D. Carsey, Observations of the late-summer to fall transition with the 14.6 GHz SEASAT scatterometer, *Proc. IGARSS '91 Symposium*, Vol. 3, IEEE Catalog #CH2971-0, June 3-6, 1991, Espoo, Finland, 1597-1600, 1991.

Drinkwater and Liu - "Seasonal -Interannual Variability in Antarctic Sea-Ice Surface Melt"

Drinkwater, M.R., and C. Haas, Snow, Sea-ice and Radar Observations during ANT X/4: Summary Data Report, *AWI Berichte aus dem Fachbereich Physik*, 53, Alfred Wegener Institut für Polar- und Meeresforschung, July 1994, 58pp., 1994.

Drinkwater, M.R., and V.I. Lytle: ERS 1 Radar and Field-Observed Characteristics of Autumn Freeze-Up in the Weddell Sea, *J. Geophys. Res.*, Vol. 102, No. C6, 12593-12608, 1997.

Drinkwater, M.R., D.G. Long, and D.S. Early, Enhanced Resolution Scatterometer Imaging of Southern Ocean Sea Ice, *ESA Journal*, 17, 307-322, 1993.

Drinkwater, M.R., X. Liu, D. Low, and P. Wadhams, Interannual Variability in Weddell Sea Ice from ERS Wind Scatterometer, *Proc. of a Joint ESA-Eumetsat Workshop on Emerging Scatterometer Applications - From Research to Operations*, 5-7 October 1998, ESTEC, Noordwijk, The Netherlands (ESA SP-424, Nov. 1998), 119-123, 1998a.

Drinkwater, M.R., X. Liu, and D. Low, Interannual Variability in Weddell Sea Ice from ERS Wind Scatterometer, *Proc. IGARSS '98*, Seattle, Washington, 6-10 July, 1998., IEEE Catalog # 98CH36174, Vol. 4, 1982-1984, 1998b.

Early, D.S., and D.G. Long: Resolution Enhancement of Scatterometer Data, *IEEE Trans. Geosci. Rem. Sens.*, In Press.

Gloersen, P., W.J. Campbell, D.J. Cavalieri, J.C. Comiso, C.L. Parkinson, and H.J. Zwally, Arctic and Antarctic sea ice, 1978-1987: satellite passive-microwave observations and analysis. *NASA SP-511*, Washington DC, National Aeronautics and Space Administration, 1992.

Gogineni, S.P., R.K. Moore, T.C. Grenfell, D.G. Barber, S. Digby, and M.R. Drinkwater, The Effects of Freeze-up and Melt Processes on Microwave Signatures, *In Microwave Remote Sensing of Sea Ice*, (Ed.) F.D. Carsey, American Geophysical Union, Geophysical Monograph 28, Chapter 17, 329-341, 1992.

Gordon, A.L., and Ice Station Weddell Group of Principal Investigators and Chief Scientists, Weddell Sea Exploration from Ice Station, *Eos*, 74, 121, 1993.

Lecomte P., W. Wagner, ERS Wind Scatterometer Commissioning and in-Flight Calibration, In *Proc. of a Joint ESA-Eumetsat Workshop on Emerging Scatterometer Applications - From Research to Operations*, Oct. 5-7, 1998, ESTEC, Noordwijk, The Netherlands, ESA SP-424, Nov. 1998.

Long, D.G., and M.R. Drinkwater, Cryosphere Applications of NSCAT Data, *IEEE Trans. Geosci. and Remote Sens.*, Vol. 37, 3, May 1999.

Low, D., The Validation of ERS-1 Summer SAR Data for Antarctic Summer Sea Ice, Unpublished M. Sc. Thesis, 143pp., 1995.

Martinson, D.G., and R.A. Iannuzzi, Antarctic ocean-ice interaction: implications from ocean bulk property distributions in the Weddell Gyre. In M.O. Jeffries (Ed.) *Antarctic Sea Ice: Physical Processes, Interactions and Variability*, Antarctic Research Series, 74, 243-271, American Geophysical Union, Washington, D.C., 1998.

Massom, R.A., M.R. Drinkwater, and C. Haas, Winter Snow Cover on Sea Ice in the Weddell Sea, *J. Geophys. Res.*, 102(C1), 1101-1117, 1997.

Massom, R.A., V.I. Lytle, A.P. Worby, and I. Allison, Winter Snow Cover Variability on East Antarctic Sea Ice, *J. Geophys. Res.*, 103(C11), 24837-24855, 1998.

Maykut, G.A., The Surface Heat and Mass Balance, In *The Geophysics of Sea Ice*, (Ed.) N. Untersteiner, 395-463, Plenum, New York, 1985.

Schwerdfeger, W., The climate of the Antarctic, World Survey of Climatology, Vol. 14, Climates of the Polar Regions, S. Orvig (Ed.), Elsevier, 253-355, 1970.

Stammerjohn, S., R. Smith, M.R. Drinkwater, and X. Liu, Variability in Sea-Ice Coverage and Ice-motion Dynamics in the PAL LTER Study Region West of the Antarctic Peninsula, *Proc. IGARSS '98*, Seattle, Washington, 6-10 July, 1998, IEEE Catalog # 98CH36174, Vol. 3, 1434-1436, 1998.

Stoffelen, A., and D. Anderson, Scatterometer Data Interpretation: Derivation of the Transfer Function CMOD4, *J. Geophys. Res.*, 102(C3), 5767-5780, 1997.

Tsai, W., J.E. Graf, C. Winn, J.N. Huddleston, S. Dunbar, M.H. Freilich, F.J. Wentz, D.G. Long, W.L. Jones: Postlaunch Sensor Verification and Calibration of the NASA Scatterometer, *IEEE Trans. Geosci. and Remote Sens.*, Vol. 37, 3, May 1999.

Winebrenner, D.P., E.D. Nelson, and R. Colony, Observations of Melt Onset on Multiyear Arctic Sea Ice using the ERS 1 Synthetic Aperture Radar, *J. Geophys. Res.*, 99, 11, 22425-22441, 1994.

Winebrenner, D.P., D.G. Long, and B. Holt, Mapping the Progression of Melt Onset and Freeze-up on Arctic Sea Ice using SAR and Scatterometry. In C. Tsatsoulis and R. Kwok (Eds.), *Analysis of SAR Data of the Polar Oceans*, Chapt. 7, 129-144, Springer-Verlag, Berlin, 1998.

Wordie, J.M., Shackleton Antarctic Expedition, 1914-1917: The natural history of pack ice as observed in the Weddell Sea, *Trans. Roy. Soc. Edinburgh*, 52, 795-829, 1921.

List of Figures

Figure 1. Weddell Sea map indicating, (i) numbered sample boxes for EScat and SSM/I time series data; (ii) ERS-1 SAR strips (dashed) on 11 and 14 February, 1995; (iii) RADARSAT ScanSAR strip (dot-dashed) on 28 December, 1996; and (iv) meteorological stations (triangles) situated at

Figure 2. Antarctic station air temperature data from 1992-1995 at (a) Faraday Station; (b) Marambio Station; and (b) Larsen ice shelf autonomous weather station (AWS) (data courtesy British Antarctic Survey). Gaps indicate failures in the instrumentation, in particular at the AWS.

Figure 3a. ERS-1 SAR swaths over the north-west Weddell Sea on 11 and 14 February, 1995. The large black box indicates the location of a simultaneous H.M.S. *Endurance* field experiment. White lines indicate coincident helicopter aerial photograph survey transects made across the marginal ice zone. Numbered boxes refer to sample regions shown in Figure 1.

Figure 3b. RADARSAT wide-swath SAR image acquired on 28 December 1996 (orbit 05994) adjacent to the northern Larsen Ice Shelf, on the Antarctic peninsula. Boxes indicate locations in Figure 1 (boxes 1, 13, 16, and 15), from which time series data are plotted. *Note disintegration of fast ice and the remaining Larsen A region and dark areas on the ice shelf where surface melting is active.

Figure 4. Modeling of the effects of wind speed on the weighted mean regional backscatter coefficient at 40° incidence (A), for (a) typical winter perennial ice (-8 dB); and (b) typical seasonal ice, or melting summer ice (-15 dB). The legend indicates the mean backscatter at varying ice concentrations.

Figure 5. EScat A images of the study region on (a) days 036 - 041 (5-10 February); and (b) days 045 - 050 (14-19 February), 1995. White open boxes show overlapping SAR swath locations simultaneous to the 10-15 February, 1995 H.M.S. *Endurance* field experiment. Open triangles indicate meteorological station locations.

Figure 6. Melt onset in the north-west Weddell Sea (64°S 56°W) in 1994, expressed as; (a) mean A values (σ_{ww}^0) at 3-day intervals; and (b) their time derivative. Vertical dashed line indicates the beginning of the 1995 calendar year.

Figure 7. ERS-2 scatterometer time series of A values from (a) Boxes 1, 2, 3, and 4 on the Larsen Ice Shelf, together with crosses indicating the algorithm-detected melt onset dates. (b) shows A values from boxes 15 and 20, together with local 6-day running mean Marambio air temperatures and corresponding mean 6-day NCEP latent heat fluxes (each at the same sampling interval).

Figure 8. Detection of Melt Onset in (a) ERS-2 (b) NSCAT data for the 1996-97 austral summer season.

Figure 9. NCEP 6-day mean latent heat flux contours for the Weddell Sea, Antarctica for 14 November, 1996 (Day 319).

Figure 10. Cumulative surface melt days detected by (a) ERS-2, and (b) NSCAT data in the 1996-97 austral summer season.

Figure 11. Interannual time series of EScat values from (a) box 9 and (b) box 22. The upper panels show the mean A values, with dotted lines indicating 1σ standard deviation. The central panel indicates the mean seasonal cycle, and the lowermost panel shows the anomaly cycle (with seasonal cycle removed).

Figure 12. Interannual melt-onset variability for the years; (a) 1992/93; (b) 1993/94; (c) 1994/95; (d) 1995/96; (e) 1996/97.

Figure 13. Interannual cumulative melt variability for the years; (a) 1992/93; (b) 1993/94; (c) 1994/95; (d) 1995/96; (e) 1996/97.

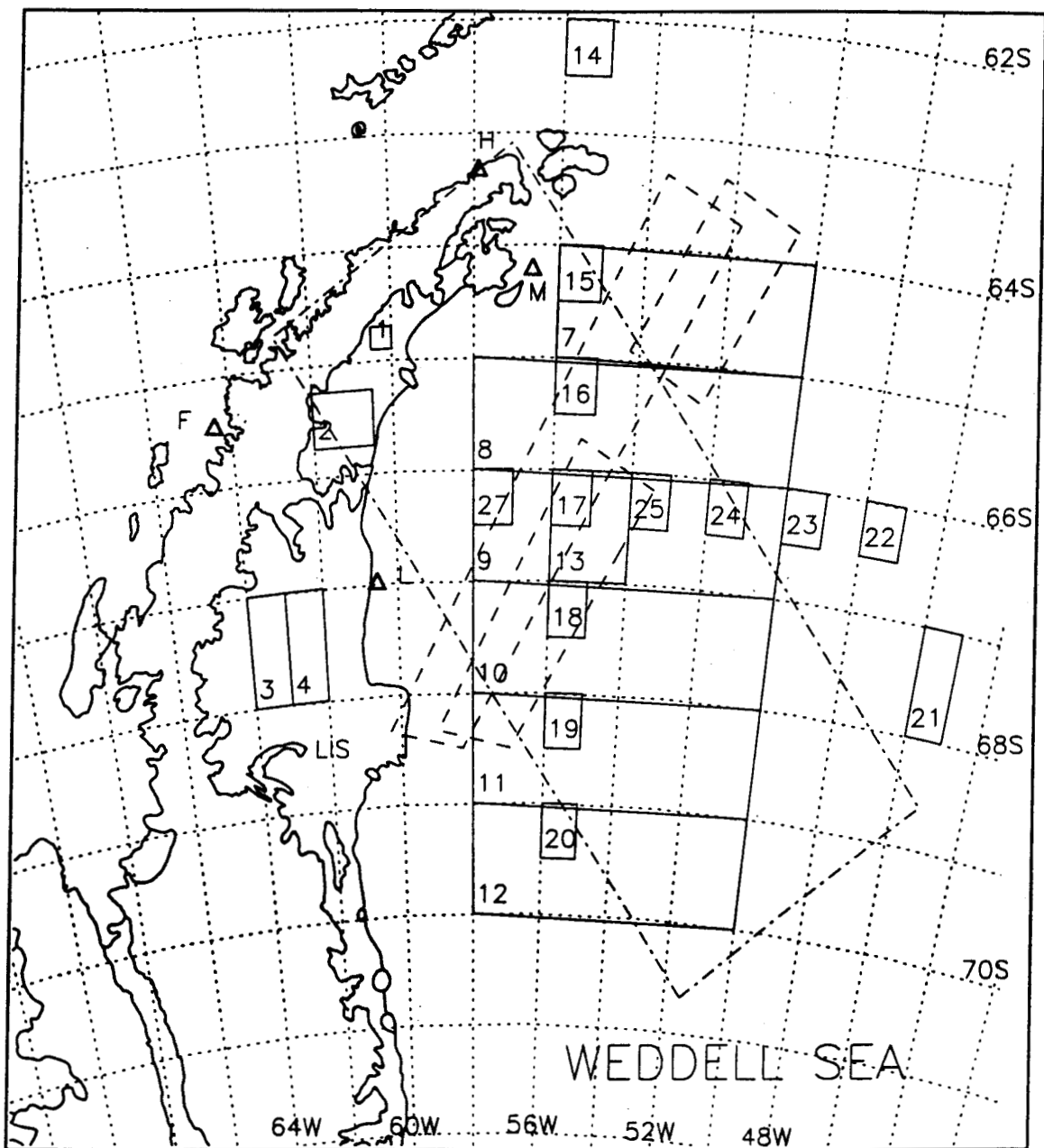


Figure 1. Weddell Sea map indicating, (i) numbered sample boxes for EScat and SSM/I time-series data; (ii) ERS-1 SAR strips (dashed) on 11 and 14 February, 1995; (iii) RADARSAT ScanSAR strip (dot-dashed) on 28 December, 1996; and (iv) meteorological stations (triangles) situated at Faraday (F), Marambio (M), and an automatic weather station on the Larsen Ice Shelf (L).

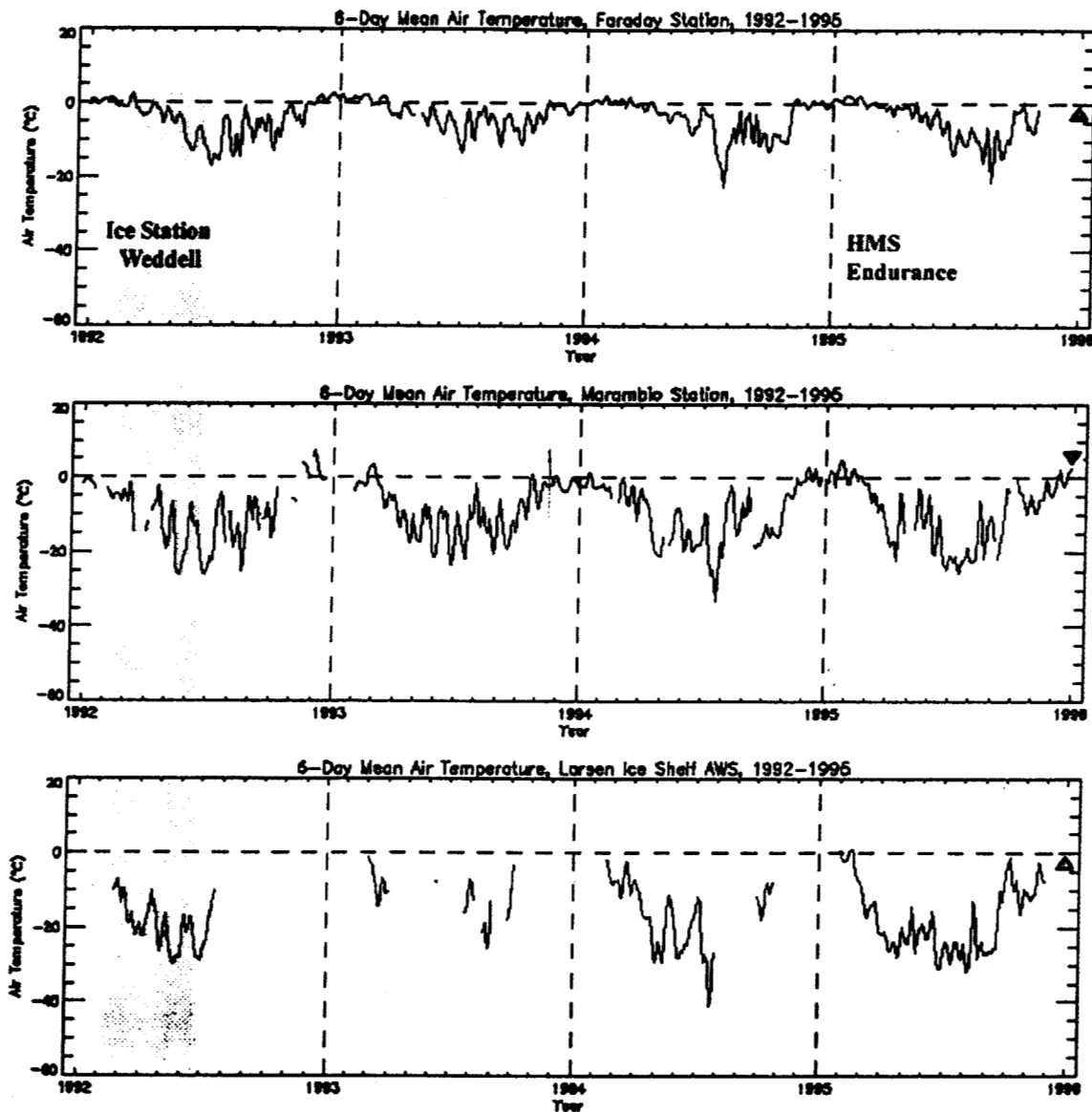


Figure 2. Antarctic station air temperature data from 1992-1995 at (a) Faraday (F); (b) Marambio (M); and (b) Larsen ice shelf (L) autonomous weather station (data courtesy British Antarctic Survey). Gaps indicate failures in the instrumentation, in particular at the AWS. Figure 1 shows the locations of these stations as solid triangles. Shaded regions indicate periods of in-situ data, and triangular symbols indicate timing of RadarSat SAR image acquisition shown in Fig. 3.

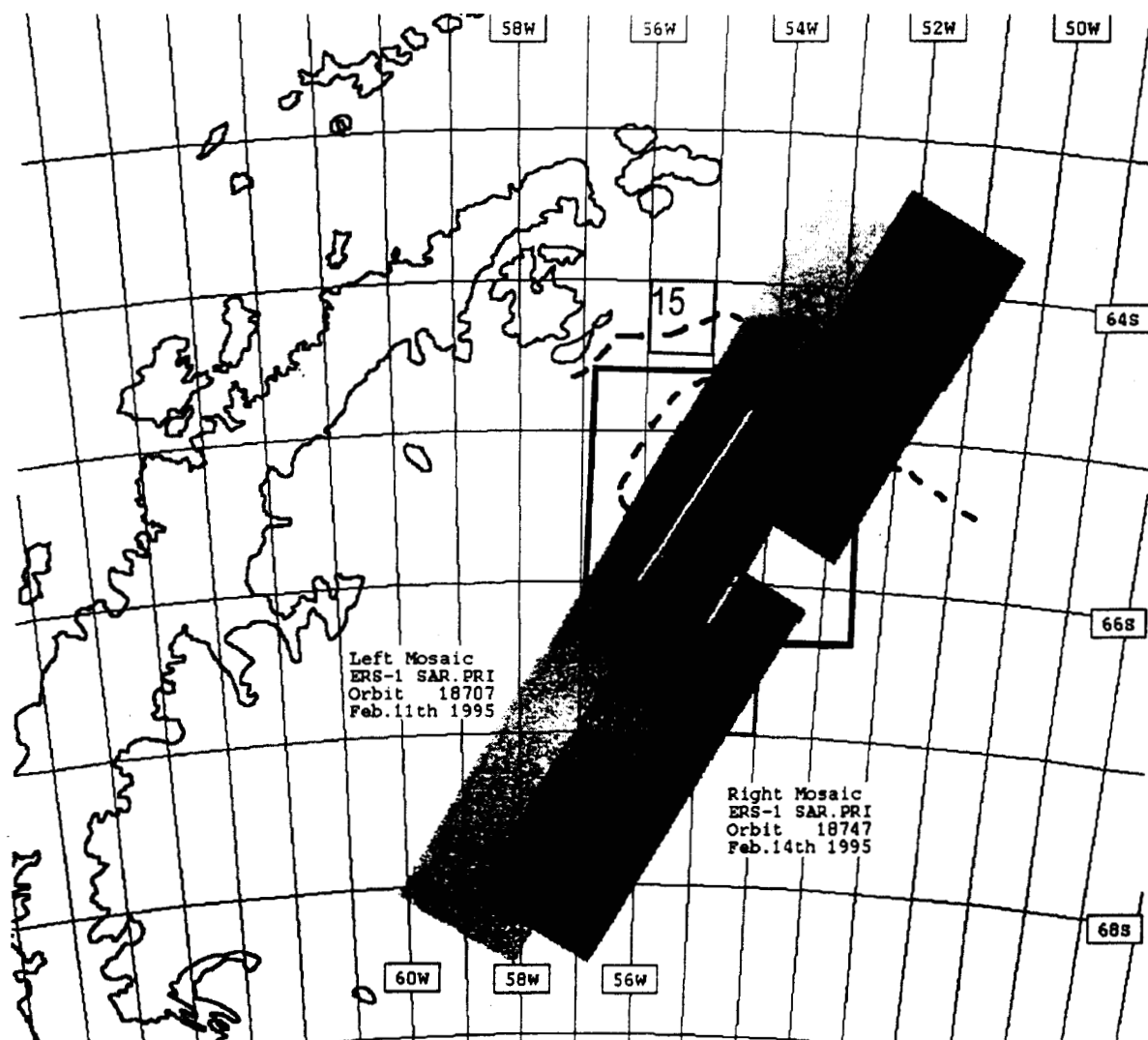


Figure 3a. ERS-1 SAR swaths over the north-west Weddell Sea on 11 and 14 February, 1995. The large black box indicates the location of a simultaneous H.M.S. *Endurance* field experiment. White lines indicate coincident helicopter aerial photograph survey transects made across the marginal ice zone. Numbered boxes refer to sample regions shown in Fig. 1.

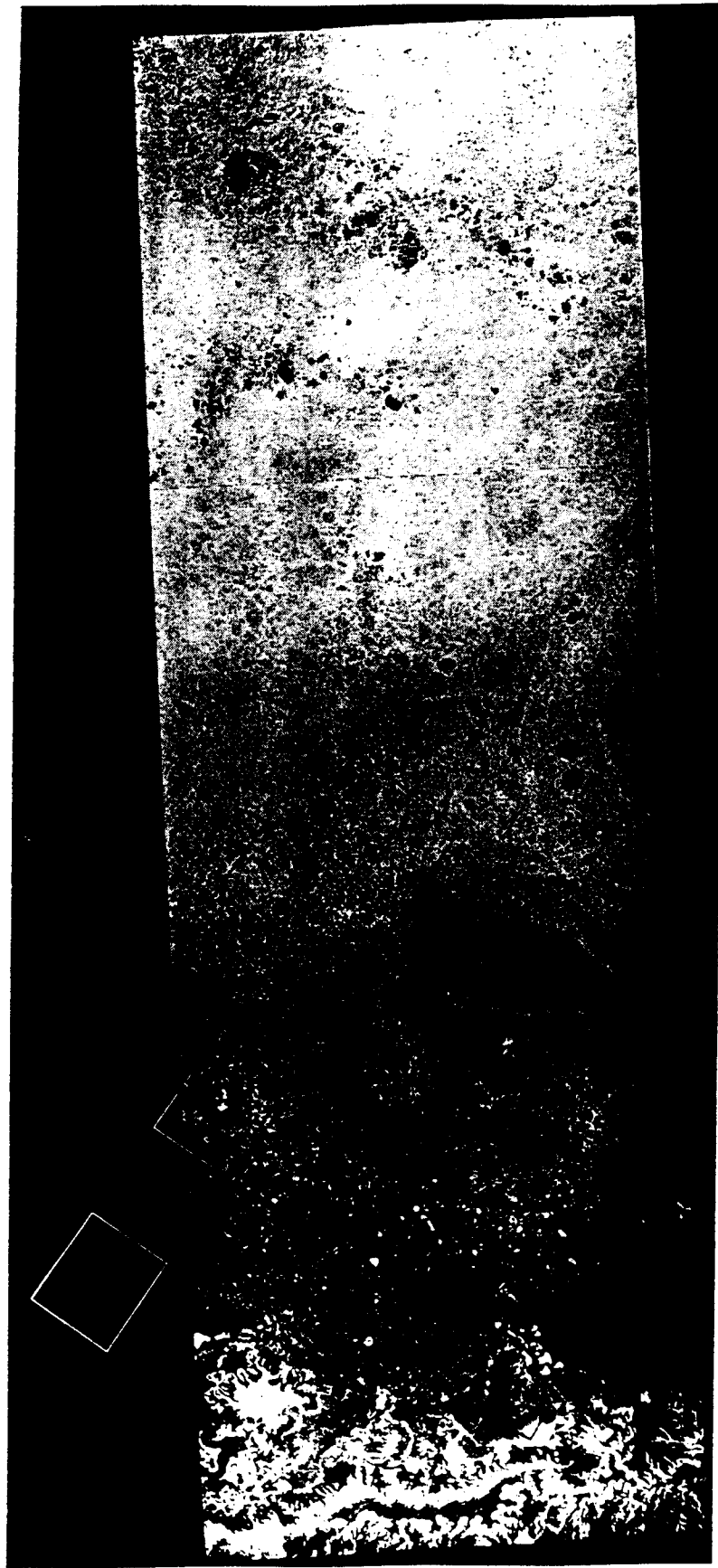


Figure 3b. RADARSAT wide-swath SAR image acquired on 28 December 1996 (orbit 05994) adjacent to the northern Larsen Ice Shelf, on the Antarctic peninsula. Boxes indicate locations in Fig 1 (boxes 1, 13, 16, and 15), from which time-series data are plotted.
*Note disintegration of fast ice and the remaining Larsen A region and dark areas on the ice shelf where surface melting is active.

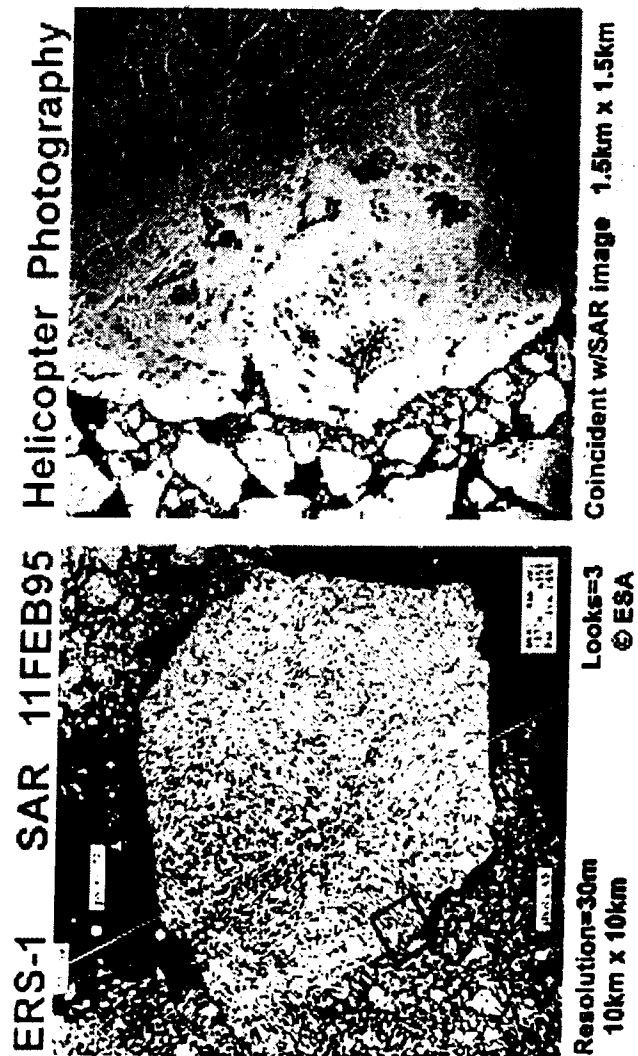
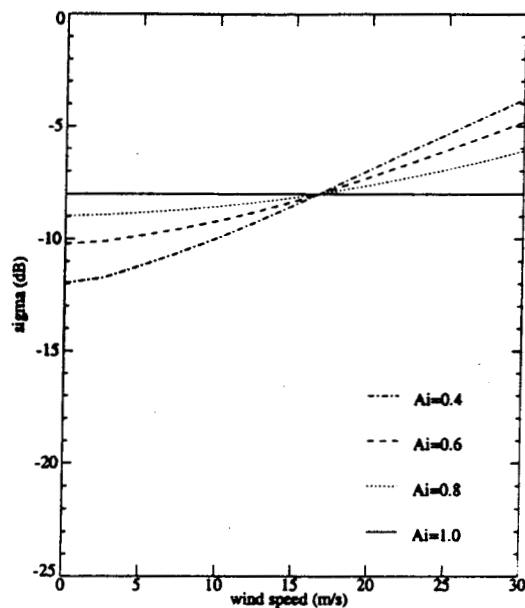


Figure 3c. ERS-1 SAR sub-image (left panel) from Fig 3a mosaic; and coincident aerial photograph (right panel) from black box indicating surface melt ponding.

a.



b.

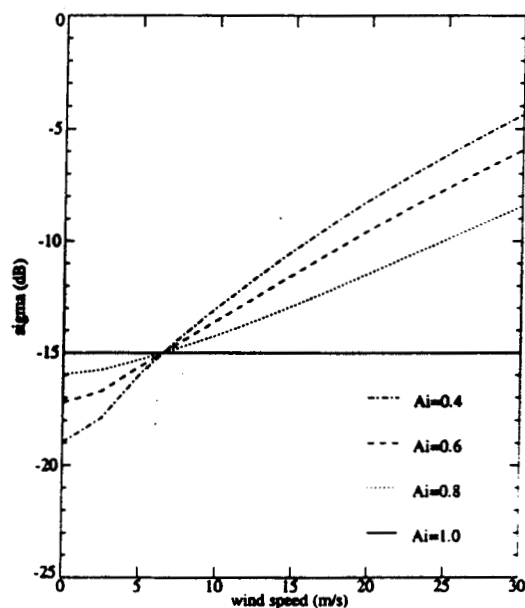
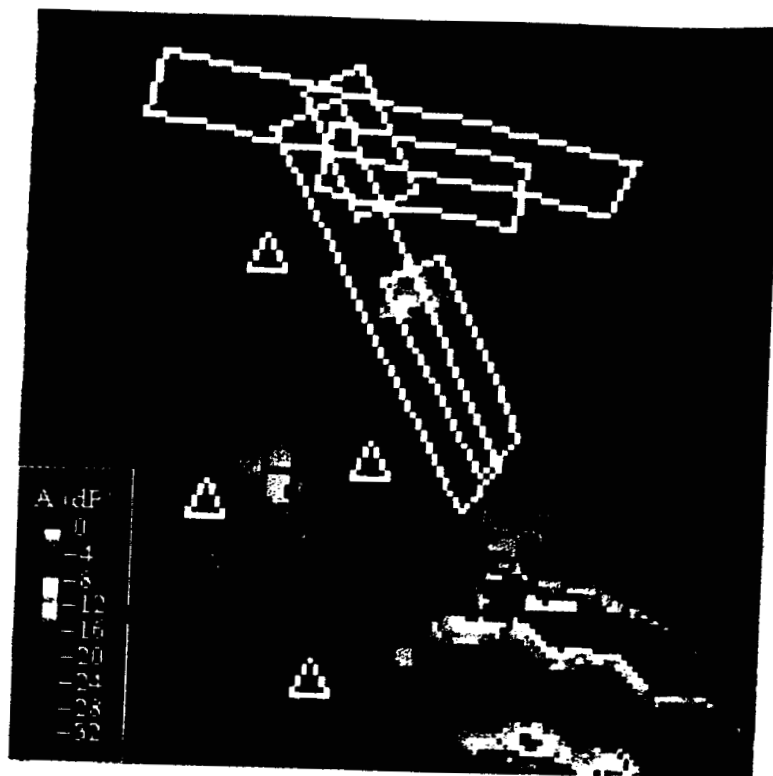


Figure 4. Modeling of the effects of wind speed on the weighted mean regional backscatter coefficient at 40° incidence (A), for (a) typical winter perennial ice (-8 dB); and (b) typical seasonal ice, or melting summer ice (-15 dB). The legend indicates the mean backscatter at varying ice concentrations.

a.



b.

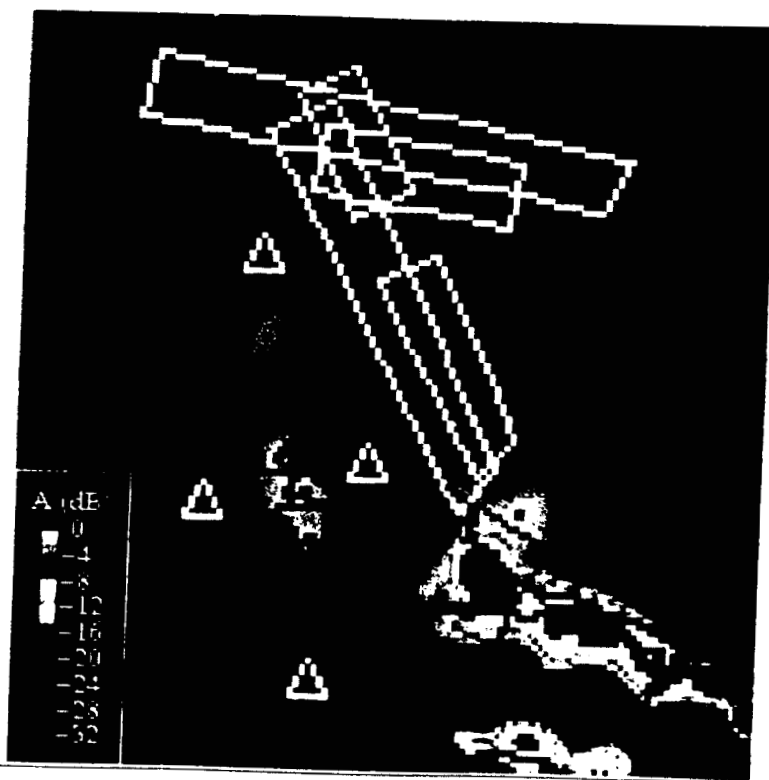


Figure 5. EScat A images of the study region on (a) days 030 - 041 (5-10 February); and (b) days 045 - 050 (14-19 February), 1995. White open boxes show overlapping SAR swath locations simultaneous to the 10-15 February, 1995 H.M.S. *Endurance* field experiment. Open triangles indicate meteorological station locations.

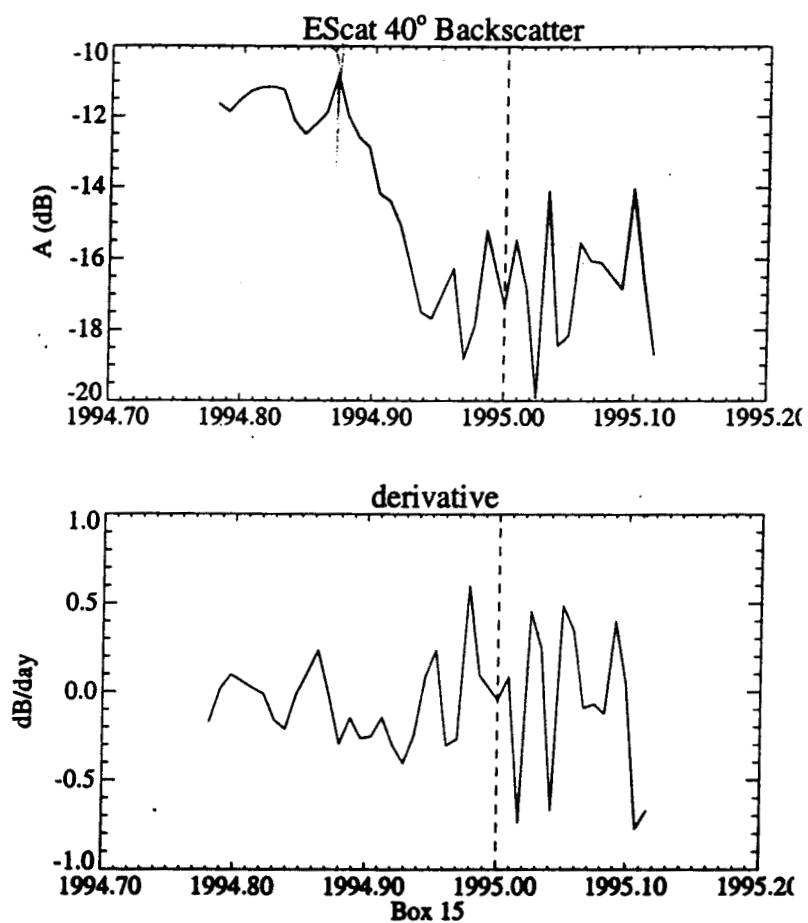
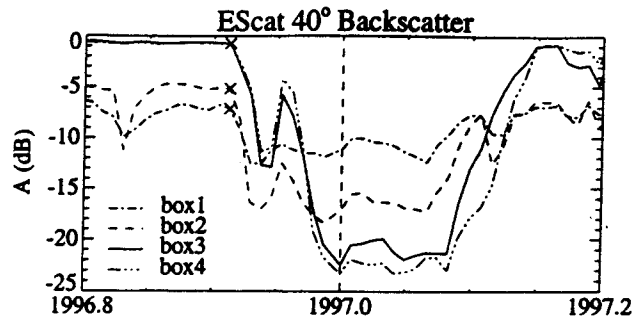


Figure 6. Melt onset in the north-west Weddell Sea (64°S 56°W) in 1994, expressed as; (a) mean A values (σ_w^0) at 3-day intervals; and (b) their time derivative. Vertical dashed line indicates the beginning of the 1995 calendar year.

a.



b.

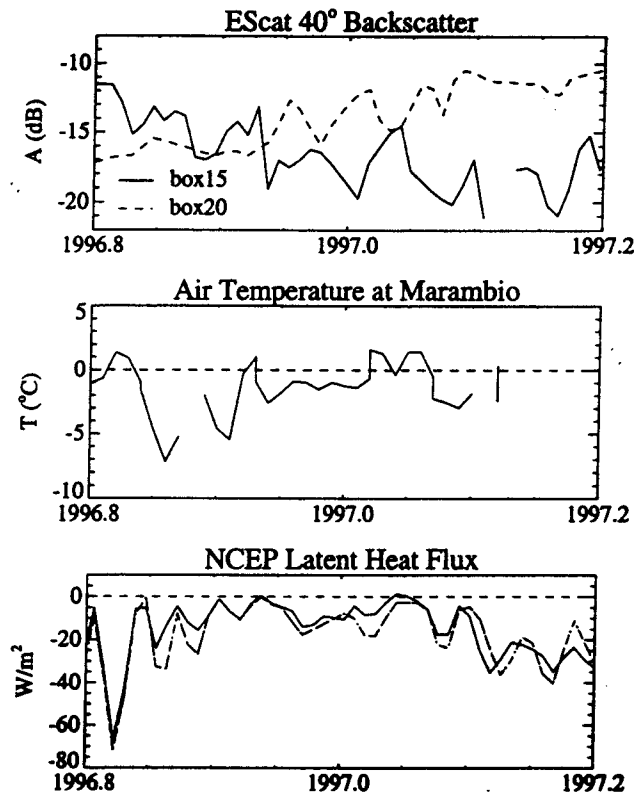
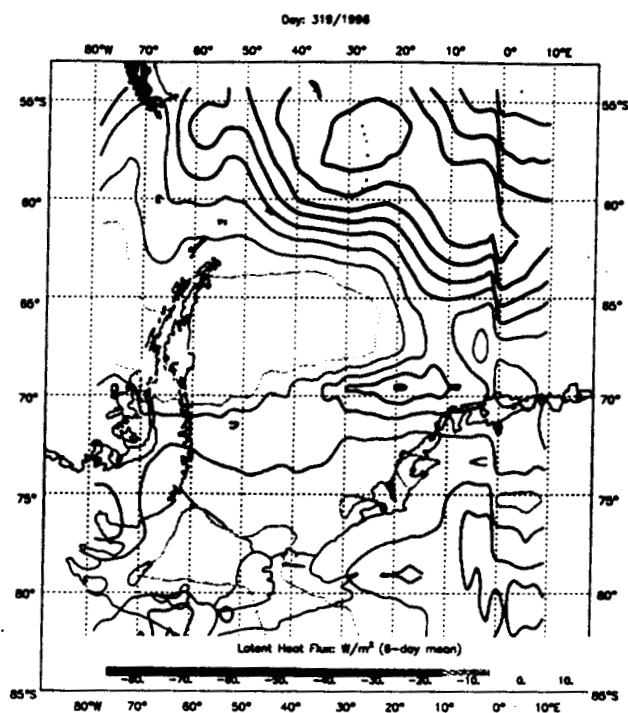


Figure 7. ERS-2 scatterometer time-series of A values from (a) Boxes 1, 2, 3, and 4 on the Larsen Ice Shelf, together with crosses indicating the algorithm-detected melt onset dates. (b) shows A values from boxes 15 and 20, together with local 6-day running mean Marambio air temperatures and corresponding mean 6-day NCEP latent heat fluxes (each at the same sampling interval).



Figure 2. Detection of Melt Onset in (a) ERS-2 (b) NSCAT data for the 1996-97 austral summer season.

(a)



(b)

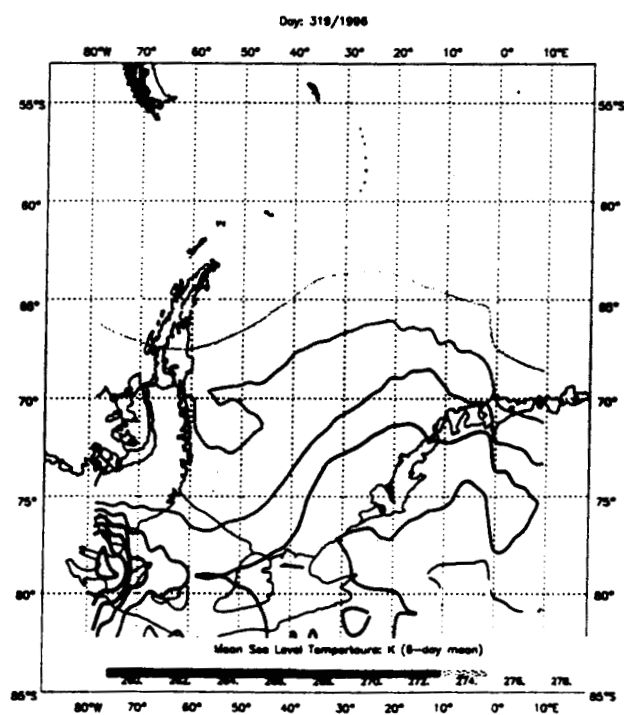


Figure 9. (a) NCEP 6-day mean latent heat flux contours; and (b) surface air temperature contours in the Weddell Sea, Antarctica, on 14 November, 1996 (Day 319).

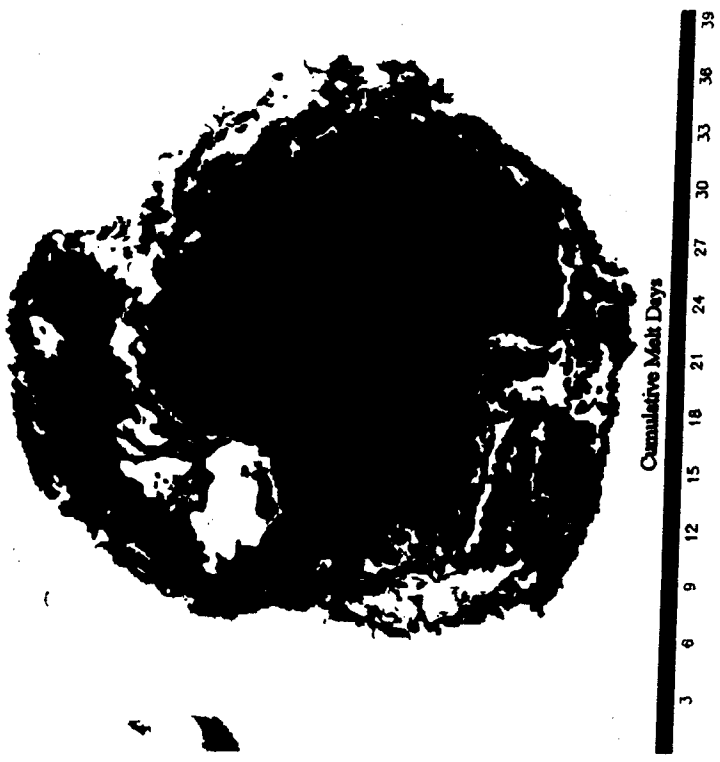
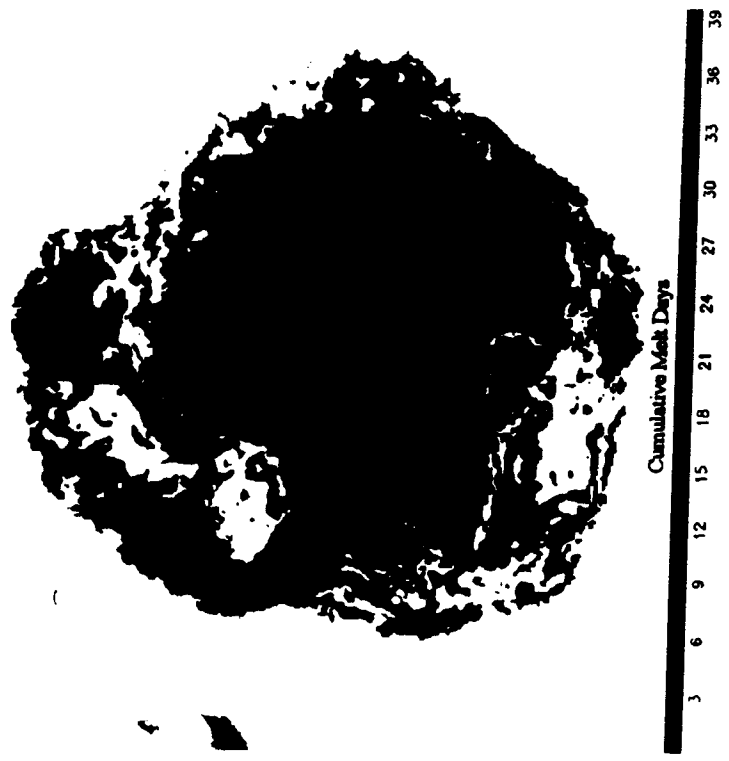
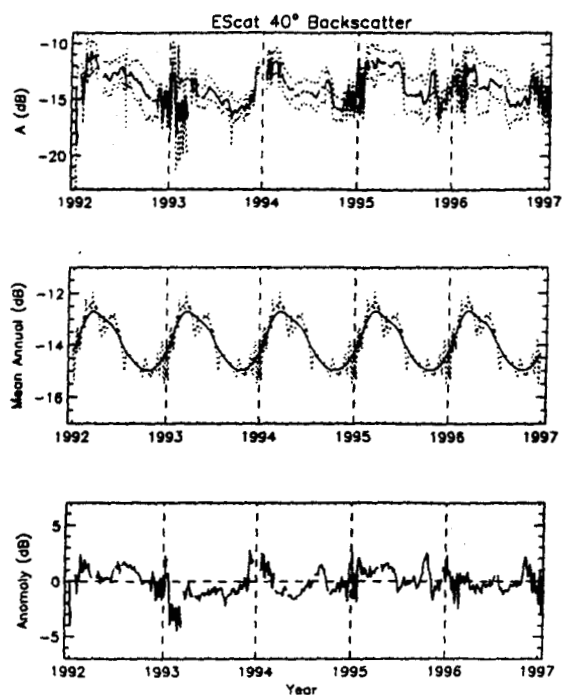


Figure 10

a.



b.

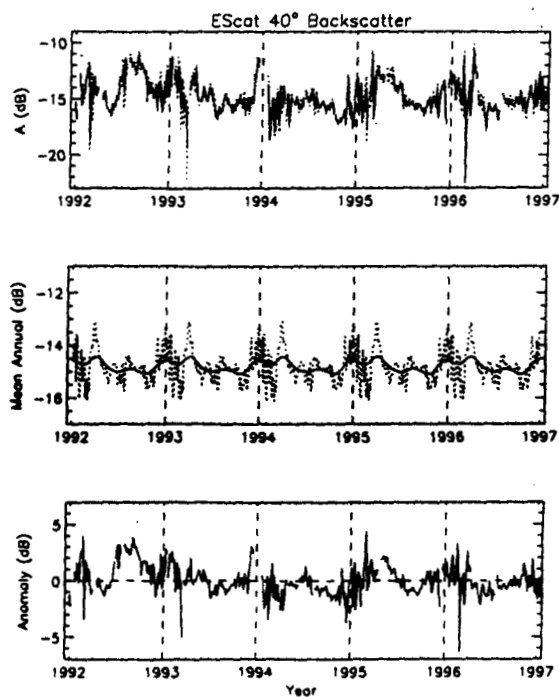
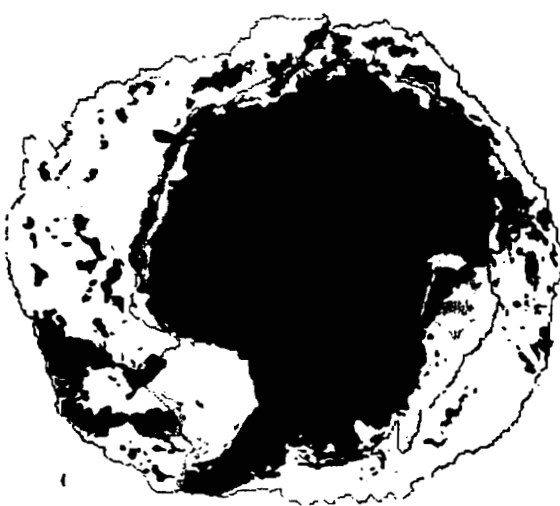
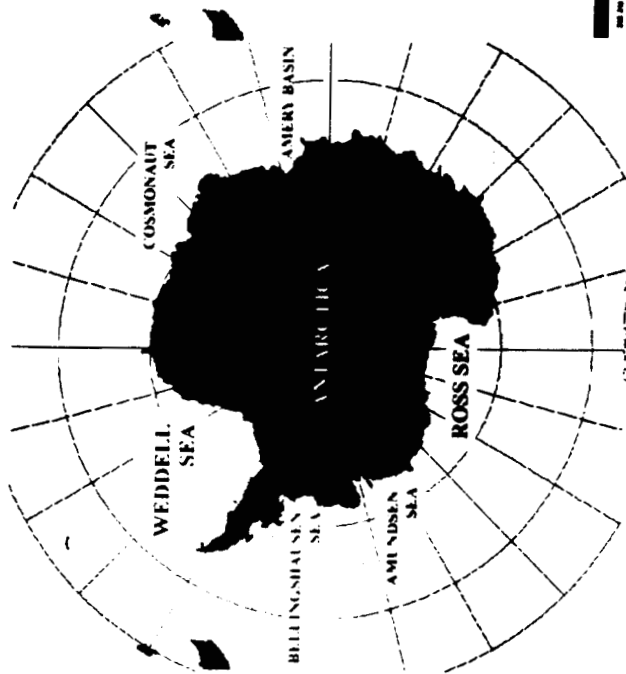
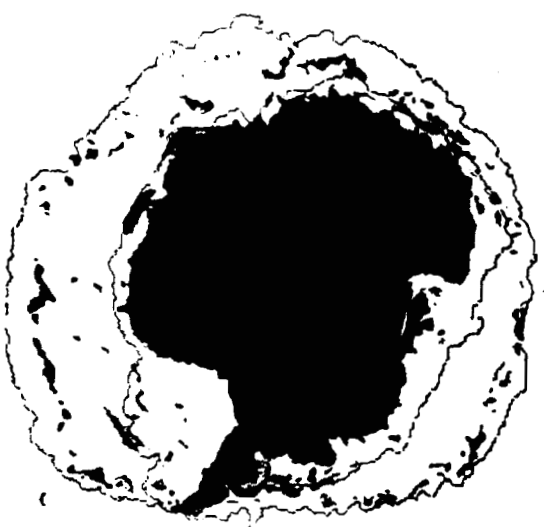


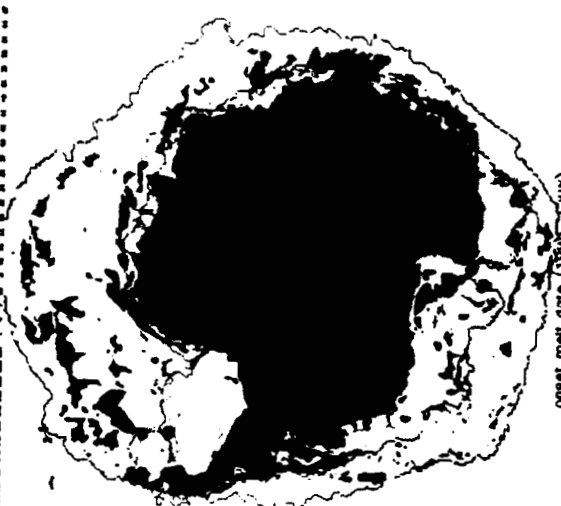
Figure 11. Interannual time-series of EScat values from (a) box 9, and (b) box 22. The upper panel in each plot shows the mean A values, with dotted lines indicating 1 σ standard deviation. The central panel indicates the mean seasonal cycle, and the lowermost panel shows the anomaly cycle.



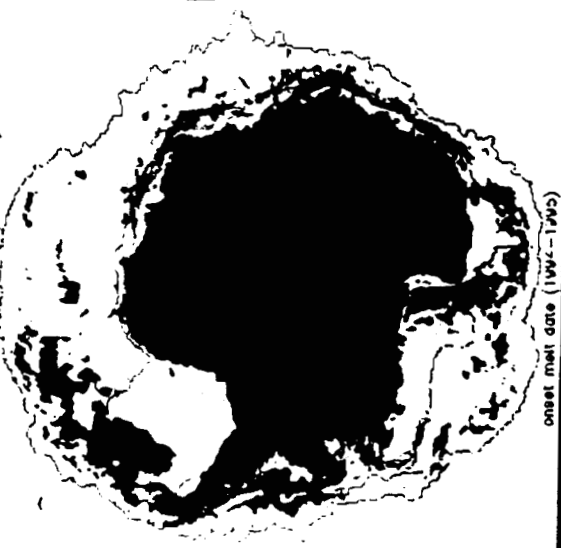
onset melt date (1992-1993)



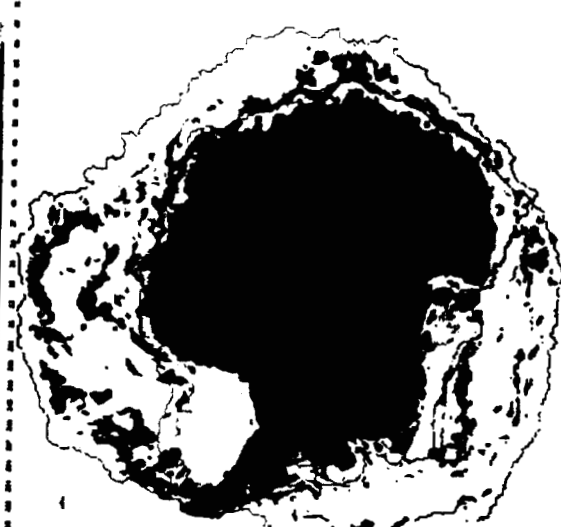
onset melt date (1993-1994)



onset melt date (1995-1996)



onset melt date (1997-1998)



onset melt date (1999-2000)

